Understanding photoluminescence of bismuth-doped ternary alkaline earth d^{10} metal oxides via first-principles calculations

Zhaoyang Feng and Chang-Kui Duan*

CAS Key Laboratory of Microscale Magnetic Resonance, and School of Physical Sciences, University of Science and Technology of China, Hefei 230026, China

and CAS Center for Excellence in Quantum Information and Quantum Physics, University of Science and Technology of China, Hefei 230026, China

(Received 31 October 2022; revised 20 January 2023; accepted 15 February 2023; published 27 February 2023)

Bismuth-activated light emissions have been much reported in ternary alkaline earth d^{10} metal oxides, and the self-activation nature of these hosts makes it possible to achieve efficient luminescence via energy transfer between the host and the activator ions. A detailed analysis of the potential intrinsic defects accounting for the intrinsic emissions is still absent, and the identifications of bismuth-related transitions remain unclear or controversial. Given these facts, first-principles calculations using hybrid functionals are employed to systematically study the bismuth-doped (Sr/Ca)Sb_2O_6, (Sr/Ca)$_2Sb_2O_7$, (Sr/Ca)SnO_3, and (Sr/Ca)Ga_2O_4, which contain d^{10} metals belonging to VA, IVA, and IIIA groups, respectively. Primary intrinsic defects and self-trapped holes in these hosts are revealed and the roles played by them on intrinsic emissions are evaluated. Bismuth ions are identified as trivalent dopants and their $^3P_{0,1} \rightarrow {}^1S_0$ (referred to as A-band) transition is assigned to account for the ultraviolet emission observed in bismuth-doped (Sr/Ca)Sb_2O_6, while the visible emission observed in (Sr/Ca)Sb_2O_6:Bi is attributed to Bi^{3+} dopants in the minute amount of (Sr/Ca)$_2Sb_2O_7$ impurities. In $Sr_2Sb_2O_7$ and $Ca_2Sb_2O_7$ with bismuth, the excitation bands are identified as $^1S_0 \rightarrow {}^3P_{0,1}$ transition of Bi^{3+}, and the observed emission bands are attributed to charge transfer transition ($Bi^{2+} + h^+_{VBM} \rightarrow Bi^{3+}$) and A-band transition ($^3P_{0,1} \rightarrow {}^1S_0$), respectively. Furthermore, the bismuth-related transitions are also well identified in (Sr/Ca)SnO_3 and (Sr/Ca)Ga_2O_4 and the large Stokes shifts of the A-band transition in (Sr/Ca)Ga_2O_4 are revealed and analyzed. The insights gained in this work extend our understanding of the properties of intrinsic defects and the luminescence mechanisms of insulating bismuth-doped ternary oxides.

DOI: 10.1103/PhysRevB.107.085144

I. INTRODUCTION

The post-transition metal bismuth with the electron configuration of [Xe] $4f^{14}5d^{10}6s^26p^3$ exists in a variety of oxidation states from -3 to $+5$ in solids, among which the most stable tripositive Bi^{3+} has been given the most attention. The less shielded outer $6s^2$ electron configuration of Bi^{3+} is sensitive to the coordination environments. As a result, wide wavelength range spans from ultraviolet to orange can be observed in Bi^{3+}-doped materials depending on the type of host compounds [1–5]. The Bi^{3+} ion has a $6s^2$ outer electron configuration with $^1S_0$ ground state, the excited states of Bi^{3+} ion include $^3P_{0,1,2}$ triplet and $^1P_1$ singlet states originating from the $6s^16p^1$ electron configuration. The optical transitions from the $^1S_0$ ground state to the $^3P_1$, $^3P_2$, and $^1P_1$ excited states are usually denoted as A, B, and C bands, respectively. The $^1S_0 \rightarrow {}^1P_1$ (C band) is a spin-allowed electric dipole transition, whereas $^1S_0 \rightarrow {}^3P_{0,2}$ are spin forbidden. The A-band transition ($^1S_0 \leftrightarrow {}^3P_1$) becomes partially spin allowed due to mixing of the triplet $^3P_1$ with singlet $^1P_1$ states via spin-orbit coupling (SOC). The radiative transition from the metastable $^3P_0$ state can occur due to mixing of the $^3P_1$ and $^3P_0$ states by the vibronic interaction with the nontotally symmetric vibrations or by the hyperfine interaction. At low temperatures ($T \ll 100$ K), the radiative emission mainly arises from the lowest-energy metastable level corresponding to the $^3P_0$ level, as the temperature increases, the emission spectrum is shifting to higher energies due to the thermally stimulated population of the higher $^3P_1$ excited level from the lower $^3P_0$ level. Considering the energy difference ΔE between the metastable level $^3P_0$ and emitting level $^3P_1$ is small, i.e., ~0.1 eV, we will make no distinction between $^3P_0$ and $^3P_1$ but use the symbol "$^3P_{0,1}$" as a generic term in the following. Except for the interconfigurational transition, i.e., $6s^2 \leftrightarrow 6s^16p^1$, the charge transfer (CT) processes between the bismuth ion and the host, i.e., metal-to-metal charge transfer (MMCT) transition ($Bi^{3+} \leftrightarrow Bi^{4+} + e^-_{CBM}$) and CT transition ($Bi^{3+} \leftrightarrow Bi^{2+} + h^+_{VBM}$) [6], are also common luminescence phenomena.

Apart from the role of acting as an activator, Bi^{3+} has also been used as a sensitizer in lanthanide ions-activated luminescent materials [7–10]. The versatile properties and nontoxic nature of Bi^{3+} ion make it promising in lighting [11,12], bioimaging [13], fiber lasers, and amplifier applications [14]. For example, multiple strategies to approach high-efficiency luminescence controllable in (blue/cyan/green)-emitting Bi^{3+}-activated phosphors is reported recently [15]; high thermal stability blue-emitting phosphors of Bi^{3+}-activated $Na_2Y_2B_2O_7$ is synthesized [16];

*ckduan@ustc.edu.cn

Bi^{3+}-doped $Cs_2Ag_{1-x}Na_xInCl_6$ exhibits efficient and stable white-light emission and is a promising white-light-emitting phosphor [17,18]; the single Bi^{3+}-doped [(Y,Sc)](Nb, V)O_4 allows for tunable emission spanning from blue to orange-red under 340–420 nm excitation, which indicates its potential application in ultraviolet (UV) excited white-light-emitting diodes [19]; a general methodology to the rational design of thermally stimulated 1.06-μm Nd^{3+} emission for the second bioimaging window demonstrated by the energy transfer from Bi^{3+} in La-, Ga-, Y-, and $LuPO_4$ is reported [20]; tunable emission from greenish to blue via chemical composition modulation in solid solutions $(Sr_{1-y}Ca_y)_2Sb_2O_7$:Bi^{3+} under near-UV light excitation is also reported [21]; a cladding-pumped bismuth-doped fiber laser is demonstrated [22].

As an important class of host materials, the ternary alkaline earth d^{10} metal oxides (hereafter referred to as d^{10} MOs), i.e., gallates, germanates, antimonates, indates, and stannates, have been adopted decades ago to study the luminescence properties of Bi^{3+} ions [23–27], and the scientific interest in the luminescence from Bi^{3+} ion based on oxides containing d^{10} metals has maintained a steady increase in recent years [21,27–38]. The UV and green emissions were observed in $SrSb_2O_6$:Bi^{3+} while the $CaSb_2O_6$:Bi^{3+} reported the UV and blue emissions [24,25,27–29,31,33,35]; the greenish emission and blue emission were reported in $Sr_2Sb_2O_7$:Bi^{3+} and $Ca_2Sb_2O_7$:Bi^{3+}, respectively [21,30]; the UV and visible (VIS) emissions were observed in both bismuth-doped strontium and calcium stannates [34,37,38]; an asymmetric band peaked at 504 nm was observed under 330-nm excitation in $SrGa_2O_4$:Bi^{3+} [32]. The above-mentioned d^{10} MOs span several crystal systems, some of which contain two or more potential sites that can be occupied by bismuth dopants. As a result, the features of reported bismuth-related transitions are quite diverse, and ambiguities and controversies exist in the assignments of optical transitions. Moreover, intrinsic emissions also emerge as a common luminescence phenomena in these hosts. For example, VIS and UV emissions were reported in pristine strontium metantimonates [25]; an orange emission peaked at 654 nm [39] and a broad blue emission peaked at 440 nm were observed in $Ca_2Sb_2O_7$ [40]; the $SrSnO_3$ and $CaSnO_3$ both exhibited a broad blue emission band [41,42]; the broad blue emission with similar features were also reported in both $SrGa_2O_4$ and $CaGa_2O_4$ [43,44]. There are also some reports on the spectral properties tuning by manipulating compositions of the hosts: the redshift phenomenon was observed when doping Sr^{2+} ions in the $Ca_2Sb_2O_7$ [45]; similarly, the tunable emission from greenish to blue via chemical composition modulation in solid solutions $(Sr_{1-y}Ca_y)_2Sb_2O_7$:Bi^{3+} was also reported [21]. In addition to these photoluminescence processes, afterglow phenomena are also reported in some cases: the yellow long persistent luminescence and mechanoluminescence were reported in $CaGa_2O_4$:Pr^{3+}, Li^+ [46]; a new cyan long afterglow phosphor $CaSnO_3$:Lu^{3+} was successfully synthesized [47].

Despite such rich luminescence phenomena reported in d^{10} MOs, theoretical studies on the luminescence mechanisms are still lacking. For the purpose of better understanding of the luminescence mechanisms of the d^{10} MOs, we carried out first-principles calculations based on density functional theory (DFT) on intrinsic defects and bismuth dopants and their excited-state properties for (Sr/Ca)Sb_2O_6, (Sr/Ca)$_2Sb_2O_7$, (Sr/Ca)SnO_3, and (Sr/Ca)Ga_2O_4. These systems are diverse enough in composition, structure, and luminescent properties, the studies may help reveal the luminescence mechanisms in d^{10} MOs and, at the same time, serve as a test of the effectiveness of first-principles calculations on a broad range of Bi-containing oxide systems.

II. METHODOLOGY

A. Computational details

The starting crystal structure data of the host crystals were taken from the Inorganic Crystal Structure Database (ICSD) [48]. The Vienna *ab initio* simulation package (VASP) was used to perform the calculations [49–52]. The Sr ($4s^24p^65s^2$), Ca ($3s^23p^64s^2$), Sb ($5s^25p^3$), Sn ($4d^{10}5s^25p^2$), Ga ($3d^{10}4s^24p^1$), O ($2s^22p^4$), and Bi ($5d^{10}6s^26p^3$) were treated as valence electrons, and their interactions with the cores were described by the projector augmented wave method [53]. The primitive cells of (Sr/Ca)Sb_2O_6, (Sr/Ca)$_2Sb_2O_7$, (Sr/Ca)SnO_3, and (Sr/Ca)Ga_2O_4 contain 9, 22, 20, and 56 atoms, respectively. The supercells with new base vectors $(2\mathbf{a}+2\mathbf{b}, \mathbf{a}-\mathbf{b}, 2\mathbf{c})$ for (Sr/Ca)Sb_2O_6 containing 72 atoms, $(\mathbf{a}+2\mathbf{b}+\mathbf{c}, \mathbf{a}+\mathbf{c}, -\mathbf{a}+\mathbf{c})$ for (Sr/Ca)$_2Sb_2O_7$ containing 88 atoms, $(\mathbf{a}+\mathbf{b}+\mathbf{c}, \mathbf{a}-\mathbf{b}+\mathbf{c}, \mathbf{a}-\mathbf{c})$ for (Sr/Ca)SnO_3 containing 80 atoms and $(-\mathbf{a}-\mathbf{b}, -\mathbf{a}+\mathbf{b}, -\mathbf{c})$ for (Sr/Ca)Ga_2O_4 containing 112 atoms were modeled to study intrinsic defects and bismuth dopants properties. Considering the facts that band edge states are involved in the intrinsic emissions and the bismuth-related charge-transfer processes in d^{10} MOs, a reasonable description of the band gaps is prerequisite and meaningful. As a result, the mixing parameters α in the hybrid functional calculations where a given ratio α of the Fock exchange is mixed with $(1-\alpha)$ of semilocal generalized gradient (GGA) functional were tuned to produce direct $\Gamma \rightarrow \Gamma$ gaps of the supercells to match the direct optical band gaps, which are determined from the spectroscopic measurements [41,43,54–59] in d^{10} MOs, so as to overcome the well-known band gap underestimation in Perdew-Burke-Ernzerhof (PBE) functional. The mixing parameters α are then determined to be 0.19, 0.20, 0.24, 0.24, 0.23, 0.19, 0.20, and 0.20 for $SrSb_2O_6$, $CaSb_2O_6$, $Sr_2Sb_2O_7$, $Ca_2Sb_2O_7$, $SrSnO_3$, $CaSnO_3$, $SrGa_2O_4$, and $CaGa_2O_4$, respectively.

Bismuth belongs to heavy metal elements and is characterized by strong SOC, where such a relativistic effect is implemented in VASP by switching on the specific tags [60] to obtain the geometric structures, the formation energies, and the transition energies of defects involving Bi atom.

The PBE functional revised for solids (PBEsol) [61] with an energy cutoff of 520 eV was used for better accuracy in optimizing the lattice constants of the primitive cells (which are fixed in calculating band structures and constructing supercells) and the calculation of dielectric tensors. A combination of PBE functional with a kinetic energy cutoff of 400 eV was adopted for the formation energies' calculations of the large amount of intrinsic defects and bismuth dopants (SOC included) in the hosts. Hybrid functional calculations (including SOC for Bi dopants) with a kinetic energy cutoff of 400 eV for the plane-wave basis were used throughout this work for the

rest calculations as a compromise of accuracy and computational costs. The mesh of k point was generated by the VASPKIT tool [62] with spacing $\sim 0.03 \times 2\pi/\text{Å}$ in all three directions for the primitive cells, and the k path in the Brillouin zone going between the high-symmetry k points for the band structure calculations are generated via the SEEK-PATH package [63,64], and the special k points in the k path for host materials are provided in Table S1 of the Supplemental Material [65]. A single Γ point was applied to sample the Brillouin zone of the supercells. To reassure readers, $CaSb_2O_6$ and $CaSnO_3$ are taken as examples to check the convergence of the k-point sampling on the Bi_{Ca} dopants and V_{Ca}. The energy differences between the defected supercells and the pristine supercell and the thermodynamic charge transition levels change relative to the results of the Γ-point calculations by less than 0.1 eV. Detailed presentations are provided in the Appendix. Therefore, we consider our calculation results to be converged. The equilibrium structures were obtained by optimizing atomic positions until the energy change was less than 10^{-6} eV and the Hellmann-Feynman forces on atoms were less than 0.01 eV/Å. The predicted lattice constants of primitive cells are only different by ∼0.5% from published experimental data (see Table S2 [65] for detailed comparison).

The dielectric tensors are indispensable for the correction scheme of the defect formation energies discussed in this study. Both ion-clamped dielectric tensors and ionic contributions to the dielectric tensors were calculated with density functional perturbation theory [73,74]. The ion-clamped electric part includes local field effects within DFT. The ionic part was calculated with a finite different scheme [75].

The spin multiplicity setting complemented with the constrained occupancy method were used here to obtain the equilibrium geometric configurations and energies of the excited states based on the hybrid functional calculations. With equilibrium configurations of both the ground and excited states obtained, the excitation and emission energies were calculated as the total energy differences (ΔSCF) between the excited and ground states of vertical transitions following the Frank-Condon principle.

B. Defect formation energy and thermodynamic charge-state transition levels

The formation energy of a defect X in the charge state q is defined as follows [76]:

$$E^f[X^q](E_F) = E_{tot}[X^q] + E_{corr}[X^q] - E_{tot}[\text{bulk}] - \sum_i n_i\mu_i + qE_F. \quad (1)$$

Here, $E_{tot}[X^q]$ is the uncorrected total energy of the supercell containing the defect, and $E_{tot}[\text{bulk}]$ is the total energy of the equivalently shaped pristine supercell of the host. The integer n_i indicates the number of atoms of type i (host atoms or impurity atoms) that have been added to ($n_i > 0$) or removed from ($n_i < 0$) the supercell to form the defect, and the μ_i are the corresponding chemical potentials of these species. The chemical potential μ_i represents the energy per atom of the reservoirs with which the system exchange atoms. E_F is the Fermi energy, i.e., the chemical potential of the electrons. The correction term E_{corr} accounts for the image charge correction and the potential alignment term between the host and charged defect supercell. The corrections which extend the method due to Frysoldt, Neugebauer, and van de Walle to anisotropic medium (eFNV) were used via the code developed by Kumagai to account for the finite-size effects [77–79]. We note that although some supercells we modeled contain only 72 atoms for $(Sr/Ca)Sb_2O_6$, and 80 atoms for $(Sr/Ca)SnO_3$, they still have a linear dimension $L = V^{1/3} \sim 10$ Å as listed in Table S3 [65], which are reasonable considering the computationally demanding fully noncollinear hybrid functional calculations and, moreover, the calculation results of Ref. [80] show that the formation energies and relative vertical transition levels (VTLs) of the defects considered were accurately corrected with eFNV method even in a 64-atom supercell. Nonetheless, we here still choose the relatively small supercells of $CaSb_2O_6$ and $CaSnO_3$ as examples to check the size convergence of the energy differences between the defected supercells and the pristine supercell and the thermodynamic charge transition levels for Bi_{Ca} dopants and V_{Ca} to reassure readers, with detailed presentations provided in the Appendix. The changes of the corrected energy differences and charge transition levels of Bi_{Ca} dopants and V_{Ca} with respect to the supercells we adopted are at the order of 0.1 eV in both $CaSb_2O_6$ and $CaSnO_3$. Therefore, the calculation results based on the supercells adopted here can be considered as reasonable in both convergence and reliability. The calculated averaged static dielectric constants of $(Sr/Ca)Sb_2O_6$, $(Sr/Ca)_2Sb_2O_7$, $(Sr/Ca)SnO_3$, and $(Sr/Ca)Ga_2O_4$ and their corresponding point charge corrections are listed in Table S3 [65].

The thermodynamic charge transition level $\varepsilon(q_1/q_2)$ is defined as the value of Fermi energy where the formation energies of charge states q_1 and q_2 are equal. From Eq. (1), we obtain

$$\epsilon(q_1/q_2) = \frac{E^f[X^{q_1}](0) - E^f[X^{q_2}](0)}{q_2 - q_1}. \quad (2)$$

C. Line shape of photoluminescence

The luminescence line shape $L(\omega)$ is uniquely determined by the spectral density of the electron-phonon coupling $S(\omega)$ and the zero-phonon line (ZPL) energy E_{ZPL}. The $S(\omega)$ depends on the coupling between lattice displacement and vibrational degrees of freedom [81]. The latter information is encoded in the so called *partial* Huang-Rhys (HR) factor

$$S_k = \frac{1}{2\hbar}\omega_k Q_k^2, \quad (3)$$

where $\hbar$ is the reduced Planck constant, and the configuration coordinate Q_k is the projection of the lattice displacement on the normalized collective displacement of phonon mode k, i.e.,

$$Q_k = \sum_\beta \sqrt{m_\beta}\left[\mathbf{n}_k^\beta | (\mathbf{R}_{e,\beta} - \mathbf{R}_{g,\beta})\right]. \quad (4)$$

Here, $\mathbf{R}_g$ and $\mathbf{R}_e$ are the atomic coordinates in the ground and excited states, while $\mathbf{n}_k$ is the normalized ionic displacement vector corresponding to phonon mode k, and m_β is the mass of atom β.

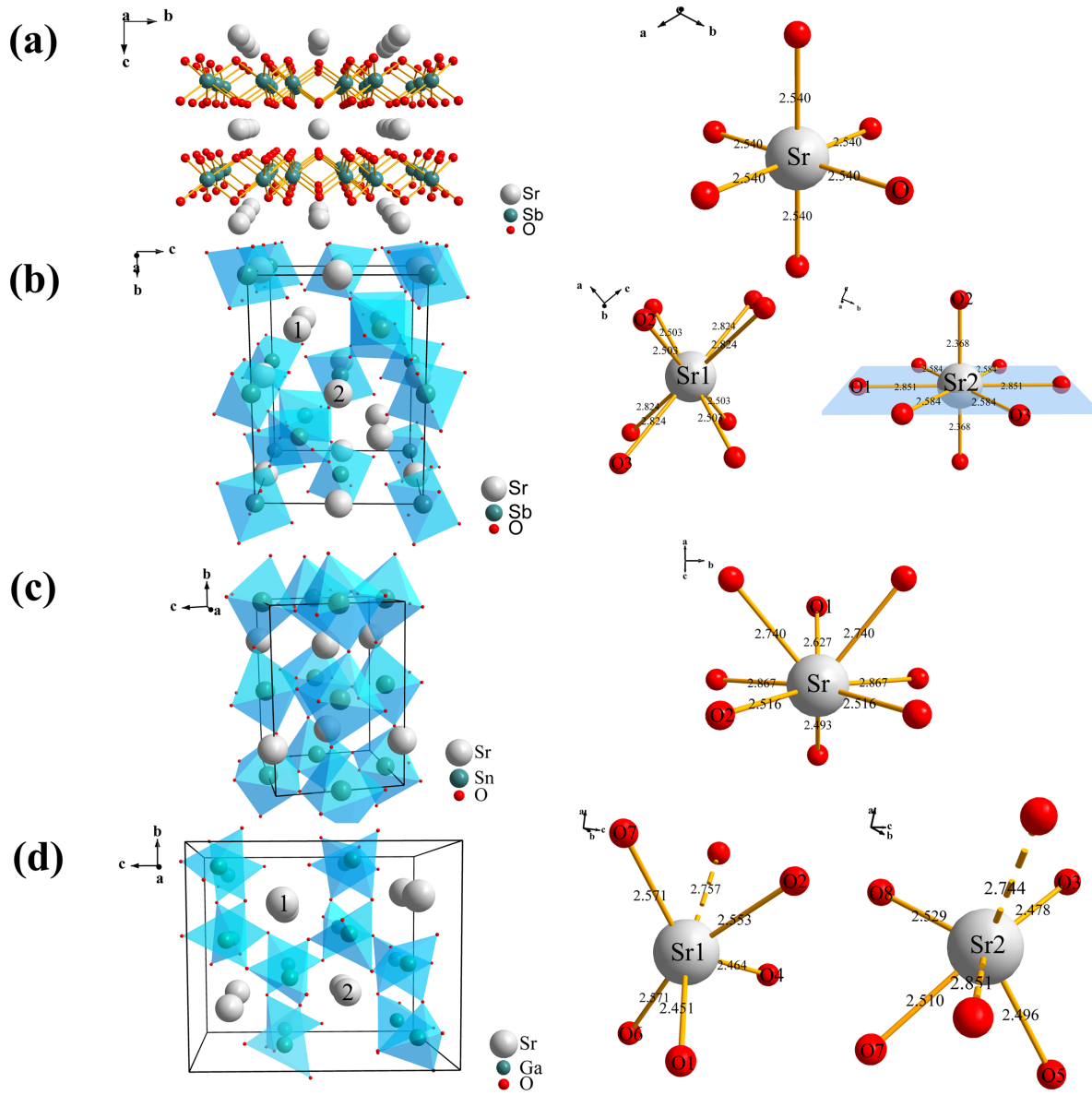

FIG. 1. Crystal structures and coordination environments of (a) $SrSb_2O_6$, (b) $Sr_2Sb_2O_7$, (c) $SrSnO_3$, and (d) $SrGa_2O_4$. Sr has a balanced local coordination environments in both bond length and angular distribution in (a) but is imbalanced in (b)–(d). Those O atoms connected to Sr via a dashed pole in (d) are generally not considered as coordinating atoms of Sr. It is noted that 1 and 2 in (b) and (d) denote Sr1 and Sr2, respectively.

The electron-phonon spectral function is then obtained by summation over all modes

$$S(\omega) = \sum_k S_k \delta(\omega - \omega_k), \tag{5}$$

where the δ functions are replaced by Gaussian with broadening parameter σ in the actual calculation. The integral over the electron-phonon spectral function gives the (total) HR factor of the transition. One possible way to determine $L(\omega)$ from the knowledge of $S(\omega)$ and E_{ZPL} is provided by means of the so-called generating function appproach [82–86]. We do not provide explicit formulas here but refer interested readers to the literature, e.g., Eqs. (7)–(12) in Ref. [86]. In the computation of the spectral density of the electron-phonon coupling $S(\omega)$, phonon spectra of the defective solids were obtained at the semilocal DFT level (PBE) using the PHONOPY package [87]. Two parameters of the broadening parameter γ that governs the width of the ZPL and the Gaussian smearing parameter σ that governs the width of the phonon sideband are both chosen to be 5 meV. The temperature T is chosen to be 300 K for a more reasonable comparison between the calculated line shapes and those measured at room temperature.

III. RESULTS AND DISCUSSIONS

A. Geometric and electronic structures of the hosts

$(Sr/Ca)Sb_2O_6$, $(Sr/Ca)_2Sb_2O_7$, $(Sr/Ca)SnO_3$, and $(Sr/Ca)Ga_2O_4$ belong to the trigonal system with the $P\bar{3}1m$ (No. 162) space group, the orthorhombic system with the *Imma* (No. 74) space group, the orthorhombic system

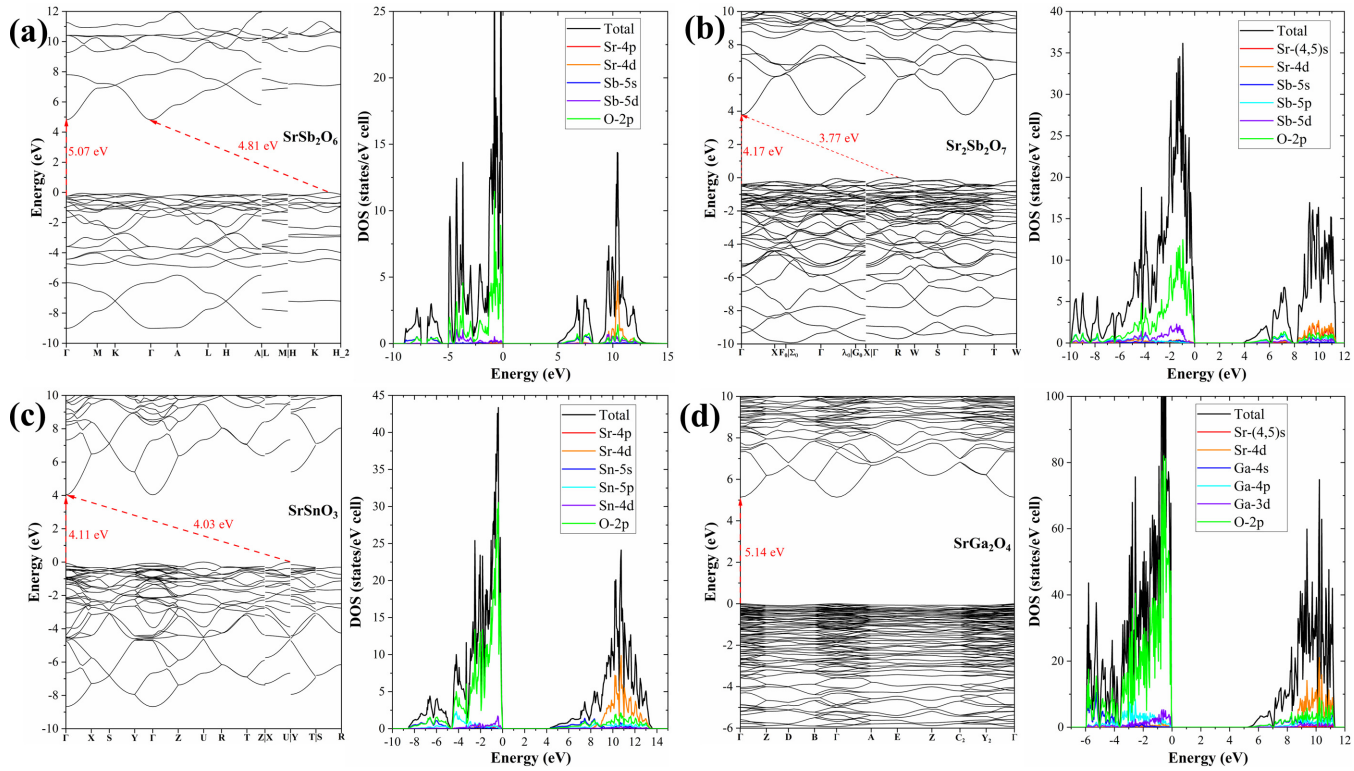

FIG. 2. Electronic band structures and DOSs of (a) $SrSb_2O_6$, (b) $Sr_2Sb_2O_7$, (c) $SrSnO_3$, and (d) $SrGa_2O_4$ calculated with hybrid functionals. The mixing parameters in hybrid functionals are 0.19, 0.24, 0.23, and 0.20 for $SrSb_2O_6$, $Sr_2Sb_2O_7$, $SrSnO_3$, and $SrGa_2O_4$, respectively.

with the *Pbnm* (No. 62) space group and the monoclinic system with the $P2_1/c$ (No. 14) space group, respectively. Figures 1(a)–1(d) correspondingly show the different relaxed crystal structures and coordination environments of strontium ion in $SrSb_2O_6$, $Sr_2Sb_2O_7$, $SrSnO_3$, and $SrGa_2O_4$. The $SrSb_2O_6$ crystal structure is made up of two-dimensional infinite sheets of edge-sharing SbO_6 octahedra alternating with layers of Sr^{2+} ion [54]. Sr atom is coordinated to six oxygen atoms forming SrO_6 octahedra. In $Sr_2Sb_2O_7$, there are two types of Sr^{2+} sites of the 4*a* and 4*d* Wyckoff positions, which are coordinated to eight oxygen ions [40]. Sr^{2+} ions in 4*d* atomic position named as Sr1 lie in a highly distorted cube with two different Sr1-O bond lengths and in 4*a* atomic position named as Sr2 in a bihexagonal pyramid with three different Sr2-O bond lengths. Sb^{5+} ions also occupy two Wyckoff positions 4*b* and 4*c* with coordination number six. SbO_6 in 4*b* atomic position exhibits a compressed octahedral structure and in 4*c* atomic position an elongated octahedral structure, while three different types of oxygen atoms, namely, O1, O2, and O3 can be found in $Sr_2Sb_2O_7$. $SrSnO_3$ exhibit an orthorhombic crystal structure, characterized by tilting and rotation of the SnO_6 octahedra, and the distorted orthorhombic perovskite structure is assembled by octahedra with shared oxygen atoms. Both Sr^{2+} and Sn^{4+} individually occupy only one crystallographic site, while two different types of oxygen atoms, namely, O1 and O2, can be found in $SrSnO_3$. $SrGa_2O_4$ possesses a distinct open structure with tunnel-like cavities running throughout the host lattice along the **a** crystal direction. The stacking of the layers along the **a** axis results in a three-dimensional framework containing channels that are occupied by the Sr cations for charge compensation. In addition, there are two crystallographically different Sr^{2+} sites, marked as Sr1 and Sr2. Sr1 ions occupy a hexahedron site with five oxygen atoms, and the average bond length is 2.52 Å; Sr2 ions occupy a tetrahedral site with four surrounding oxygen atoms, and the average bond length is 2.50 Å. The Ga atoms occupy a tetrahedral site with four coordinated oxygen atoms, while eight different types of oxygen atoms, namely, O1, O2, O3, O4, O5, O6, O7, and O8, can be found in $SrGa_2O_4$. Similar structure features are shared by their calcium counterparts and so are omitted.

Figure 2 plots the electronic band structures and density of states (DOSs) of $SrSb_2O_6$, $Sr_2Sb_2O_7$, $SrSnO_3$, and $SrGa_2O_4$ calculated by employing the hybrid functionals with their corresponding mixing parameters. The hybrid functional calculations significantly improve the band gaps, predicting direct $\Gamma \rightarrow \Gamma$ band gaps of 5.07, 4.17, 4.11, and 5.14 eV for $SrSb_2O_6$, $Sr_2Sb_2O_7$, $SrSnO_3$, and $SrGa_2O_4$, respectively. The projected DOSs show that the dominant components of the valence band edge states are O-2*p* orbitals, while the conduction band edge states are constituted by the hybridization of the *sp* orbitals of d^{10} metal ions, mixed with O-2*p* orbitals. The situation is similar for $CaSb_2O_6$, $Ca_2Sb_2O_7$, $CaSnO_3$, and $CaGa_2O_4$ (see Fig. S1 [65]). Different from the dominance of *d* orbitals of transition metal ions in the conduction bands of ternary d^0 transition metal oxides [88], the *d* orbitals of metal ions in the d^{10} MOs are stabilized into core levels due to the large nucleus fields of the d^{10} metal elements, and instead the conduction band is formed by *sp* orbitals. Large dispersion of conduction band due to the broad *sp* orbitals can generate high-mobility photoexcited electrons, suggesting the potential applications of d^{10} MOs in the field of photocatalysis [89].

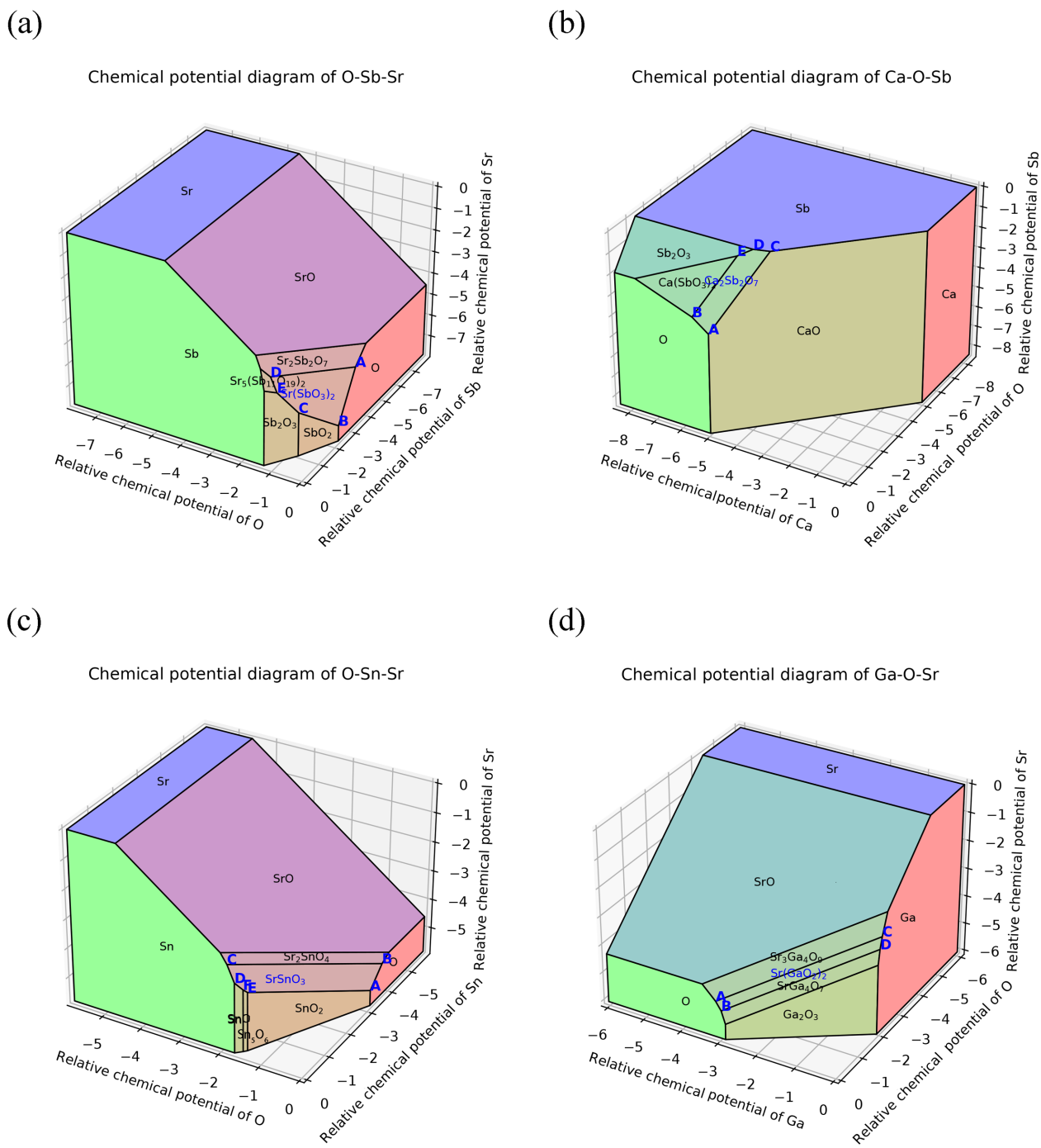

FIG. 3. The chemical potential diagrams for (a) $SrSb_2O_6$, (b) $Ca_2Sb_2O_7$, (c) $SrSnO_3$, and (d) $SrGa_2O_4$, respectively. The secondary compounds around the points are used to determine the relative chemical potentials $\Delta\mu_i$. Notes: For presentation purpose, the chemical potential of oxygen is relative to $\mu_O(p, T) = -5.92, -5.92, -5.85$, and -6.12 eV for $SrSb_2O_6$, $Ca_2Sb_2O_7$, $SrSnO_3$, and $SrGa_2O_4$, respectively, while the chemical potentials of other elements are still relative to their values in the simple substances (metals). The points A and B are selected to mimic the experimental synthesis conditions. The chemical potential values at vertices are provided in Table S4 [65].

B. Intrinsic and Bi-related defects

The commonly observed intrinsic emissions and afterglow phenomena and the much reported bismuth-activated emissions in d^{10} MOs make it necessary to study the intrinsic defect properties and the site preference of bismuth dopants in these hosts. Here, we choose $SrSb_2O_6$, $Ca_2Sb_2O_7$, $SrSnO_3$, and $SrGa_2O_4$, one of each of the four crystal systems under study, to present intrinsic defect properties and the site preference of bismuth dopants. The defect formation energy mentioned in Sec. II is an important physical quantity to characterize the intrinsic defect properties, which can be used to determine the primary intrinsic defects under corresponding thermodynamic equilibrium conditions. Defects with smaller formation energies are easier to form, and are present in higher

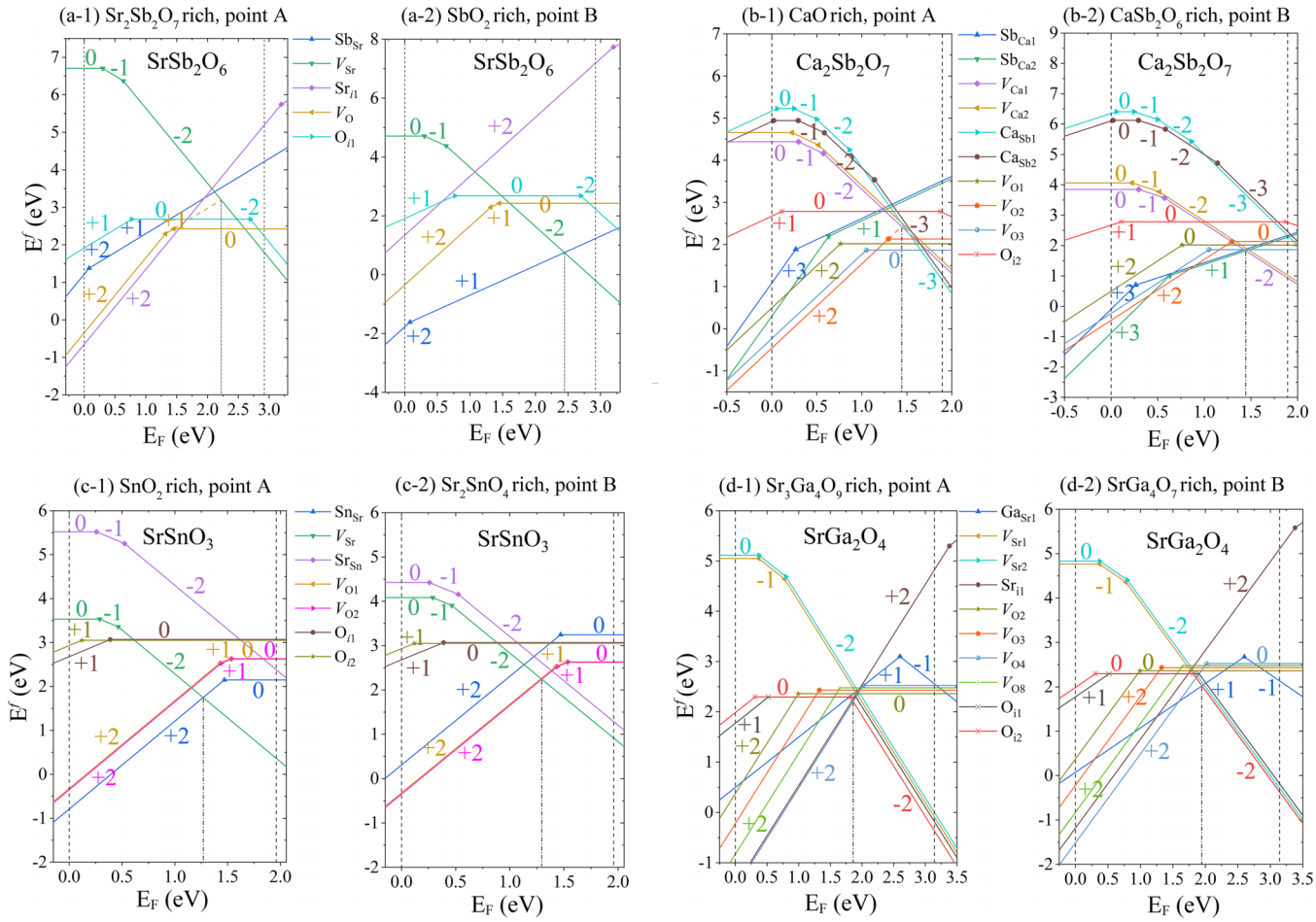

FIG. 4. Formation energies of intrinsic defects as a function of the Fermi level under (a-1) A point and (a-2) B point in $SrSb_2O_6$, (b-1) A point and (b-2) B point in $Ca_2Sb_2O_7$, (c-1) A point and (c-2) B point in $SrSnO_3$, and (d-1) A point and (d-2) B point in $SrGa_2O_4$ specified by their corresponding chemical potential diagrams in Fig. 3. The vertical dashed dot lines are the charge equilibrium Fermi level in the undoped hosts.

concentrations. Such defects are then more likely to play a role in the materials' luminescence properties.

In order to sustain the existence of stable pure phases of $SrSb_2O_6$, $Ca_2Sb_2O_7$, $SrSnO_3$, and $SrGa_2O_4$, we consider the chemical potentials μ_i at the conditions where competing phases coexist with the host materials, which are determined from the chemical potential diagrams (CPDs) shown in Figs. 3(a)–3(d) for $SrSb_2O_6$, $Ca_2Sb_2O_7$, $SrSnO_3$, and $SrGa_2O_4$, respectively. The chemical potential diagrams are generated by PYDEFECT [79], and the PYDEFECT package retrieve crystal structures of the stable competing phases from the Material Project database (MPD) during the construction of chemical potential diagram (CPD). However, out of consideration for taking the experimentally measured crystal structures as a starting point of the first-principles calculations, we replace the crystal structures of the competing phases from the MPD with those from the ICSD except for some very few phases which cannot be found in the ICSD, i.e., Sr ($R3m$, No. 166), Sn_5O_6 ($P2_1/c$, No. 14). Nevertheless, the CPD which is based entirely on the MPD is still adopted as a reference for us to choose the potential competing phases [90].

Here, the chemical potentials μ_i in Fig. 3 are specified with respect to their μ_i^0 values for the simple substances except for the chemical potential of oxygen. The chemical potential of oxygen gas is usually expressed as [91]

$$\mu_O(p,T) = \frac{1}{2}E_{O_2} + \frac{k_B T}{2}\left[\ln\frac{pV_Q}{k_B T} - \ln(Z_{rot}Z_{vib})\right], \quad (6)$$

where T is the temperature, p is the partial pressure of O_2, $V_Q = (2\pi\hbar^2/mk_BT)^{\frac{3}{2}}$ is so-called quantum volume of O_2 gas with m the mass of O_2, k_B the Boltzmann constant and $\hbar$ the reduced Planck constant, Z_{rot} and Z_{vib} are the rotational and vibrational partition functions, and E_{O_2} is the energy of an isolated O_2 molecule, which has been added 1.36 eV to correct the overbinding error in GGA-type calculations [92]. For the purpose of clear and intuitional presentation of the chemical potentials in the three-dimensional chemical potential diagrams, the chemical potential of oxygen in Fig. 3, $\Delta\mu_O$, is specified with respect to $\mu_O(p,T)$ rather than μ_O^0, half of the (corrected) total energy of an isolated O_2 molecule, while the chemical potentials of other elements for the hosts in Fig. 3 are still relative to their values in the simple substances. Considering the hosts are all synthesized by solid-state reactions under the air atmosphere with ambient oxygen partial pressure $p = 0.21$ atm and high-synthesis temperatures

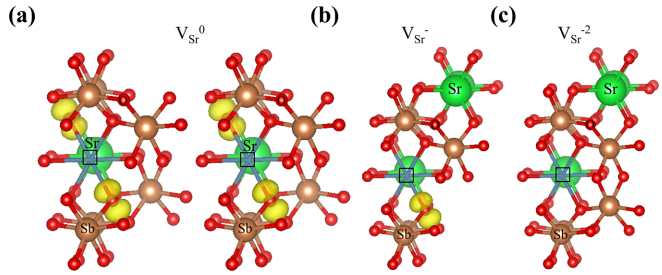

FIG. 5. Strontium vacancy in $SrSb_2O_6$ in different charge states: (a) neutral V_{Sr}^{0}; (b) singly negative V_{Sr}^{-}; (c) doubly negative V_{Sr}^{-2}. The vacancy location is indicated with an empty square. The isosurface plots of the hole wave-function squares for V_{Sr}^{0} and V_{Sr}^{-} are also shown, with the isosurfaces corresponding to 10% of the maximum. The strontium, stibium, and oxygen ions are represented with green, brownness, and red, respectively. Notes: The Sr vacancy in the neutral charge state leaves two holes in the valence band, which corresponds to two isosurface plots as shown in the figure, and the situation is similar for calcium vacancy in $CaSb_2O_6$ and is omitted here.

$T = 1423$ [35], 1423 [93], 1373 [40], and 1573 K [43] for $SrSb_2O_6$, $Ca_2Sb_2O_7$, $SrSnO_3$, and $SrGa_2O_4$, respectively, $\mu_O(p, T)$ are then determined to be -5.92, -5.92, -5.85, and -6.12 eV correspondingly by applying Eq. (6). Herein, we are only focusing on determining the primary intrinsic defects of the samples synthesized by solid-state reactions under the air atmosphere, i.e., $\Delta\mu_O = 0$ in Fig. 3. As a result, two reference chemical potential points of the reaction in air (A and B) in Fig. 3 are selected to determine the chemical potentials μ_i. The points A and B define $Sr_2Sb_2O_7$-rich and SbO_2-rich conditions, CaO-rich and $CaSb_2O_6$-rich conditions, SnO_2-rich and Sr_2SnO_4-rich conditions, and $Sr_3Ga_4O_9$-rich and $SrGa_4O_7$-rich conditions for $SrSb_2O_6$, $Ca_2Sb_2O_7$, $SrSnO_3$, and $SrGa_2O_4$, respectively. The corresponding formation energies of intrinsic defects are plotted in Figs. 4(a)–4(d) for $SrSb_2O_6$, $Ca_2Sb_2O_7$, $SrSnO_3$, and $SrGa_2O_4$, respectively. The Bi_2O_3 compound is used here to determine the upper bound of μ_{Bi}, and is adopted to calculate the reference formation energies of Bi-related defects. The chemical potential values at vertices are listed in Table S4 [65] for interested readers.

As is shown in Fig. 4(a), V_{Sr}^{2-} shows its dominance as negative intrinsic defect in $SrSb_2O_6$, especially in Fig. 4(a-2), which corresponds to the SbO_2-rich condition. The V_O^+ in Fig. 4(a-1) and the Sb_{Sr}^+ in Fig. 4(a-2) are the primary positive defects under $Sr_2Sb_2O_7$-rich and SbO_2-rich conditions, respectively. Similarly, V_{Ca1}^{2-} is also revealed as the most important negatively charged defect in $Ca_2Sb_2O_7$. In spite of the CaO-rich condition in Fig. 4(b-1), which should be favorable for the formation of Ca_{Sb1} and Ca_{Sb2} and unfavorable for the formation of V_{Ca1} and V_{Ca2}, the V_{Ca1}^{2-} still shows its dominance, and the formation energies of V_{Ca}^{2-} and Ca_{Sb}^{3-} at the pinned Fermi level do not deviate so much. The more loose structure of $(Ca/Sr)Sb_2O_6$ compared with $(Ca/Sr)_2Sb_2O_7$ make it more beneficial for the formation of interstitials, i.e., Sr_{i1} and O_{i1}, in $SrSb_2O_6$. We now turn to the $SrSnO_3$, in Fig. 4(c-1) corresponding to SnO_2-rich condition and the Fig. 4(c-2) corresponding to Sr_2SnO_4-rich condition, V_{Sr}^{2-} defects both exist as the primary negative intrinsic defects, while the Sn_{Sr}^{2+} and $V_{O1,2}^{2+}$ exist as the primary positive intrinsic defects in Figs. 4(c-1) and 4(c-2), respectively. Finally, when it comes to $SrGa_2O_4$, Figs. 4(d-1) and 4(d-2) correspond to $Sr_3Ga_4O_9$-rich and $SrGa_4O_7$-rich conditions, respectively. The O_{i2}^{2-} in Fig. 4(d-1) exists as the primary negative intrinsic

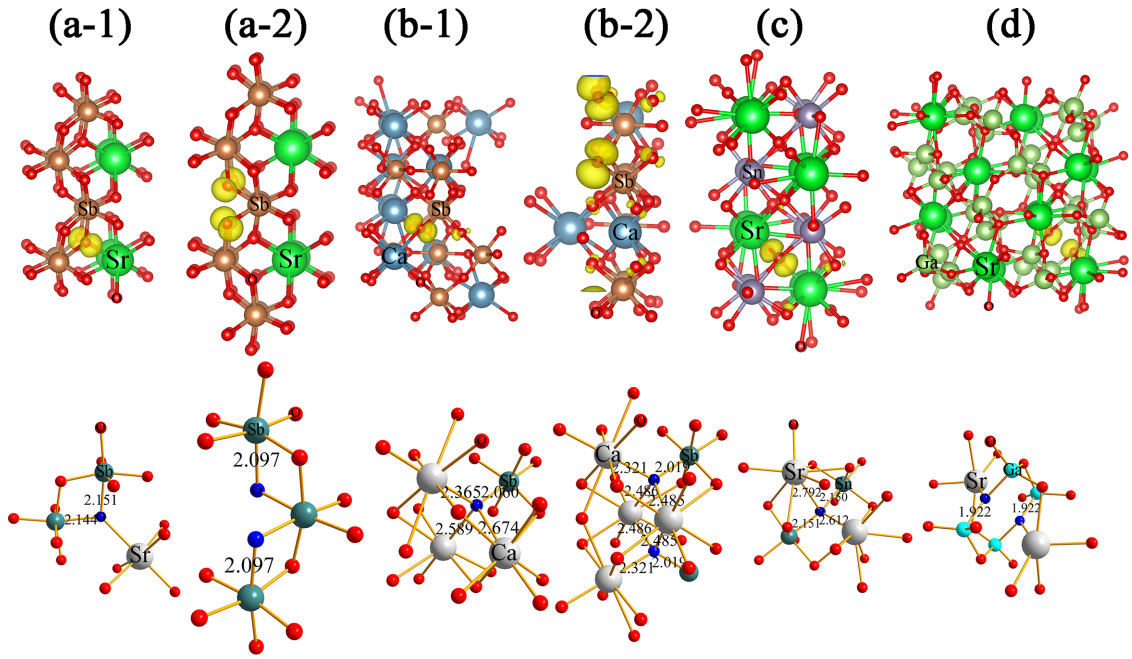

FIG. 6. STHs in (a) $SrSb_2O_6$, (b) $Ca_2Sb_2O_7$, (c) $SrSnO_3$, and (d) $SrGa_2O_4$. The isosurface plots of the hole wave-function squares are shown with the isosurfaces corresponding to 10% of the maximum. The STH is localized on an individual oxygen atom in $SrSnO_3$ while localized on two equivalent oxygen atoms in $SrGa_2O_4$ and two STH configurations [one-oxygen STH (a-1), (b-1) and two-oxygen STH (a-2), (b-2)] are found in $SrSb_2O_6$ and $Ca_2Sb_2O_7$. Notes: The blue atoms denote the oxygen ions on which the hole is localized.

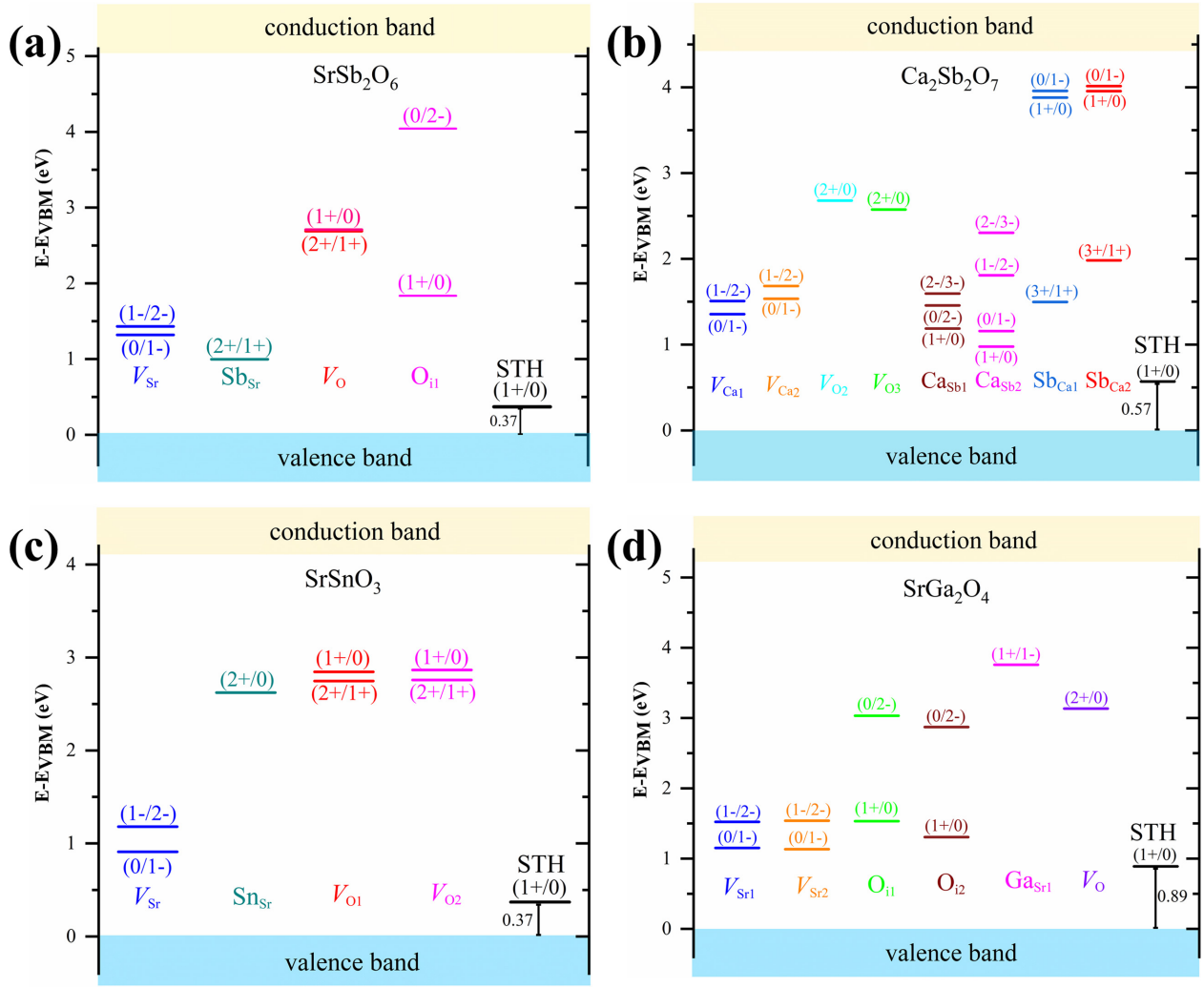

FIG. 7. The thermodynamic charge transition levels of the primary intrinsic defects and self-trapping energies of the STHs in (a) $SrSb_2O_6$, (b) $Ca_2Sb_2O_7$, (c) $SrSnO_3$, and (d) $SrGa_2O_4$.

defect while the V_{Sr1}^{2-}, V_{Sr2}^{2-}, O_{i1}^{2-}, and O_{i2}^{2-} in Fig. 4(d-2) all show their dominance as negative intrinsic defects. And V_{O4}^{2+}, Sr_{i1}^{2+}, and Ga_{Sr1}^{+} defects emerge as primary positive intrinsic defects in Figs. 4(d-1) and 4(d-2), respectively.

The site preference of bismuth dopants in $SrSb_2O_6$, $Ca_2Sb_2O_7$, $SrSnO_3$, and $SrGa_2O_4$ is also analyzed according to the formation energy calculations (Fig. S2 [65]). The bismuth dopants prefer to occupy the Sr site and Ca site as Bi^{3+} ion in $SrSb_2O_6$ and $Ca_2Sb_2O_7$, and may exist as Bi^{4+} or Bi^{5+} ion at the Sb site, both of which are inactive in luminescence. Moreover, the formation energies of the Bi_{Ca1}^{+} and Bi_{Sr2}^{+} are found to be 0.22 eV lower than those of the Bi_{Ca2}^{+} and Bi_{Sr1}^{+} in $Ca_2Sb_2O_7$ and $Sr_2Sb_2O_7$, respectively. Considering the high-temperature synthesis conditions, such a small difference in formation energies indicates that Bi^{3+} may occupy both of the two Sr (Ca) sites in $Sr_2Sb_2O_7$ ($Ca_2Sb_2O_7$). The bismuth dopants in $SrSnO_3$ substitute Sr site as Bi^{3+}, and may substitute Sn^{4+} as Bi^{3+}, Bi^{4+}, and Bi^{5+}. As for the $SrGa_2O_4$, the bismuth dopants are found to be likely to substitute both two Sr sites and Ga1 and Ga3 sites (among the four Ga sites) as Bi^{3+} ions.

C. Intrinsic defects, self-trapped holes, and their impacts on intrinsic luminescence

The formation energies of intrinsic defects in Fig. 4 reveal the dominance of the alkaline earth vacancies in the d^{10} MOs. It is also well known that Sr and Ca are ionic and their vacancies do not lead to dangling bonds. In fact, the neutral charge state of the Sr (Ca) vacancy leaves two holes in the valence band, which is derived mostly from O-2p states. The holes, in turn, prefer to become localized on separate O atoms next to the vacancy, but stay away from each other to reduce the Coulomb repulsion energy. Similar scenarios were also reported in $SrTiO_3$ [94]. The Sr (Ca) vacancy can be further stabilized in the singly negative V_{Sr}^{-} (V_{Ca}^{-}) and doubly negative V_{Sr}^{2-} (V_{Ca}^{2-}) charge states, as shown in Fig. 4. The Sr vacancies in $SrSb_2O_6$ in different charge states are shown in Fig. 5 as an example, the isosurface plots of the hole wave-function squares for Sr or Ca vacancies in different charge states in other hosts are also provided in Fig. S3 [65]. The Sr and Ca vacancies are double acceptors, showing great potential as hole trap centers in d^{10} MOs. They may act as hole trap

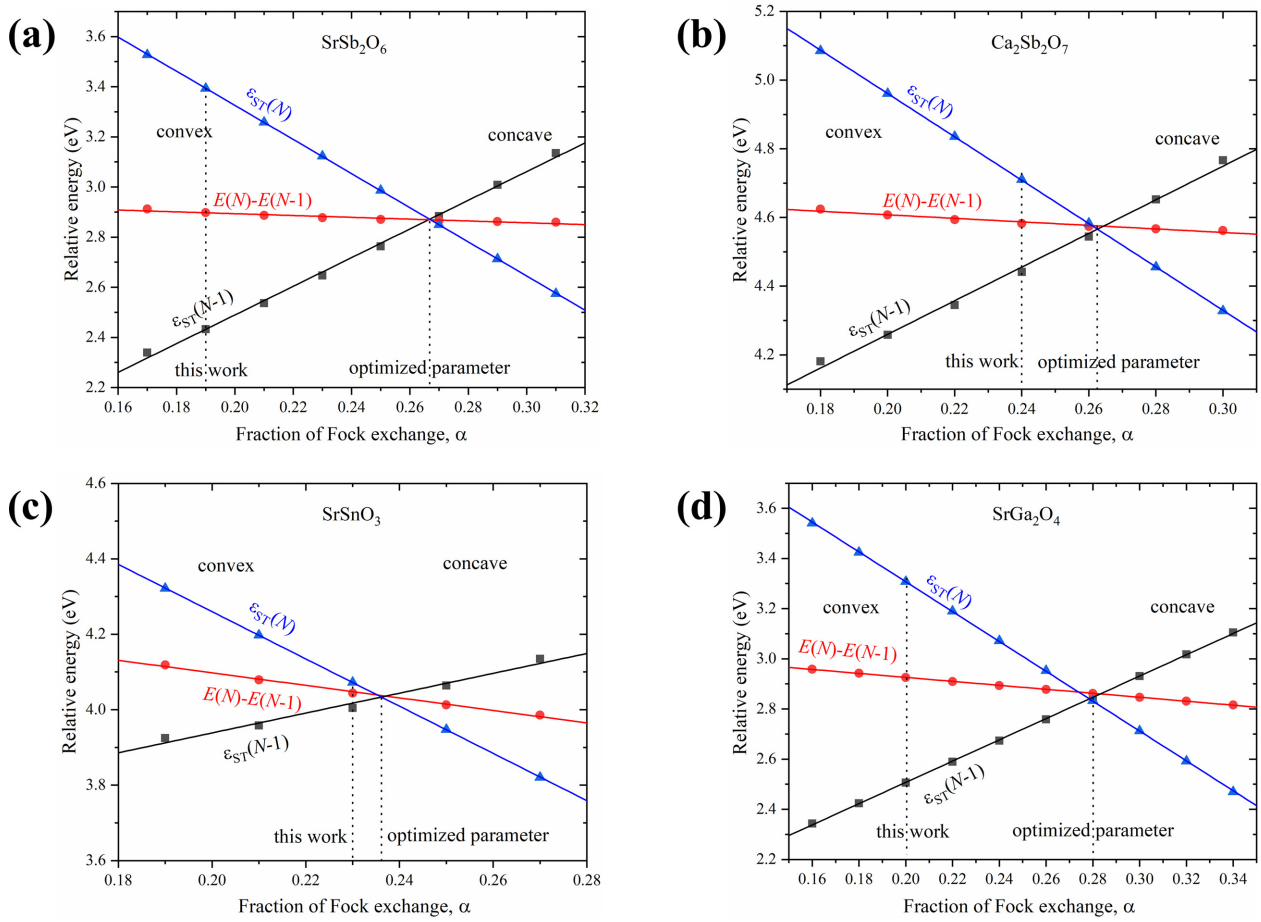

FIG. 8. Total energy difference between the neutral supercell with STH geometry and a positively charged supercell with a STH, $E[N] - E[N-1]$, and STH single-particle levels without and with an electron addition, $\varepsilon_{ST}[N-1]$ and $\varepsilon_{ST}[N]$, respectively, for the STHs in (a) $SrSb_2O_6$, (b) $Ca_2Sb_2O_7$, (c) $SrSnO_3$, and (d) $SrGa_2O_4$, respectively.

centers in the long persistent luminescence as reported experimentally [46,47,95].

It has been shown in Fig. 2 and Fig. S1 [65] that the highest of the valence bands in the d^{10} MOs are dominated by O-2p orbitals and characterized by small dispersion and high density of states, which indicate the large effective masses and low mobility of photoexcited holes in the valence bands, especially for the $SrGa_2O_4$, and the scenarios shown in Fig. 5 and Fig. S3 [65] further inspire us to consider the formation of self-trapped holes (STHs) in the d^{10} MOs. So we here investigate the formation of STHs and then evaluate their impact on optical properties of the hosts. For each of the four hosts, by removing an electron from the valence band of the supercell and starting with slightly distorted structures to avoid being stuck at a high-symmetric configurations, we obtained the stable STH geometric configurations as shown in Fig. 6. Two different configurations of the one-oxygen STH and two-oxygen STH shown in Figs. 6(a-1) and 6(a-2), respectively, are found in $SrSb_2O_6$, leading to elongations of the local Sb-O bond lengths by 7.6% $\sim$ 7.9% and 5.2%, respectively, the lowest-energy configuration is the one-oxygen STH shown in Fig. 6(a-1), which is 0.06 eV lower in total energies. Despite the small total-energy difference between the one-oxygen STH and two-oxygen STH in $SrSb_2O_6$, an energy barrier of 0.17 eV is found between them (Fig. S4 [65]). That is to say, the two-oxygen STH can emerge as a metastable configuration in $SrSb_2O_6$. Similar situation is also found in $CaSb_2O_6$ (Fig. S5 [65]). Two STH configurations of the one-oxygen STH and two-oxygen STH are also found in $Ca_2Sb_2O_7$, the one-oxygen STH is 0.14 eV lower in total energies than that of two-oxygen STH and an energy barriers of 0.15 eV is found between them (Fig. S4 [65]), which also indicate the existence of two-oxygen STH as a metastable configuration in $Ca_2Sb_2O_7$. However, the two-oxygen STH in $Sr_2Sb_2O_7$ is highly unstable and is easy to relax to the one-oxygen STH. The local Sb-O and Ca-O bonds lengths are elongated by 5.0% $\sim$ 9.5% and 3.0% $\sim$ 3.4% for the one-oxygen STH and two-oxygen STH in $Ca_2Sb_2O_7$, respectively. The hole left in the valence band becomes localized on an individual O atom for $SrSnO_3$, leading to elongations of the local Sn-O and Sr-O bonds lengths by 4.2% $\sim$ 5.6%. The two-oxygen STH in $SrSnO_3$ and $CaSnO_3$ is highly unstable and is easy to relax to the one-oxygen STH. In $SrGa_2O_4$, the structure relaxation of the STH starting from different initial configurations always results into localizing on two equivalent oxygen atoms, leading to elongations of the local

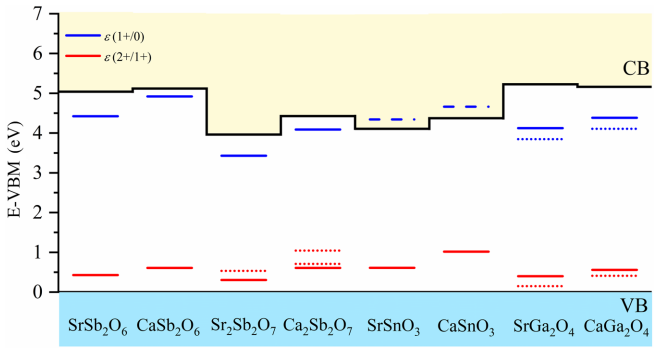

FIG. 9. The Bi^{3+} dopants induced defect levels in the band gaps of the ternary alkaline earth d^{10} metal oxides. The dotted lines represent the Bi^{+}_{Sr2}, Bi^{+}_{Ca2}, Bi^{+}_{Sr2}, Bi^{+}_{Ca2} related charge transition levels for the $Sr_2Sb_2O_7$, $Ca_2Sb_2O_7$, $SrGa_2O_4$, and $CaGa_2O_4$, respectively; the dashed lines represent the $\varepsilon(1+/0)$ thermodynamic charge transition levels of Bi^{3+} in (Ca/Sr)SnO_3, which are slightly higher than the CBMs.

Ga-O bonds length by 3.2% ∼ 4.5%. Similar situations in local environment changes are also found in their strontium or calcium counterparts (Fig. S5 [65]), which will not be repeated here.

The stability of STHs in the hosts can be characterized by the self-trapping energy E_{ST}, which corresponds to the position of $\varepsilon(+/0)$ associated with each STH, the E_{ST} or $\varepsilon(+/0)$ is given as [96]

$$E_{ST} = E_p - (E[h^+] + E_{corr}[h^+]) - \varepsilon_{VBM}, \tag{7}$$

where $E[h^+]$ and E_p are the total energies of the supercell containing a STH h^+ and the perfect crystal supercell without the defect, respectively, and ε_{VBM} denotes the energy level of the valence band maximum (VBM). The E_{ST} is calculated to be 0.37 eV ($SrSb_2O_6$), 0.57 eV ($Ca_2Sb_2O_7$), 0.37 eV ($SrSnO_3$), and 0.89 eV ($SrGa_2O_4$), as plotted in Fig. 7. The significantly large binding energy of STH in $SrGa_2O_4$ compared with those in $SrSb_2O_6$, $Ca_2Sb_2O_7$, and $SrSnO_3$ is consistent with the much smaller dispersion of the tops of valence bands for alkaline earth gallates among the four series of d^{10}-MOs under study as shown in Fig. 2. However, it is worth noting that the satisfaction of the generalized Koopmans' theorem [97] (GKT) is important for the good description of the hole polaron state, and the optimal mixing parameters determined via the satisfaction of the GKT may be quite different from those determined via the reproduction of the optical band gaps. As a result, a question arose naturally: Is it possible that the mixing parameters we adopted may lead to an artifact? Hence, it is necessary for us to determine the mixing

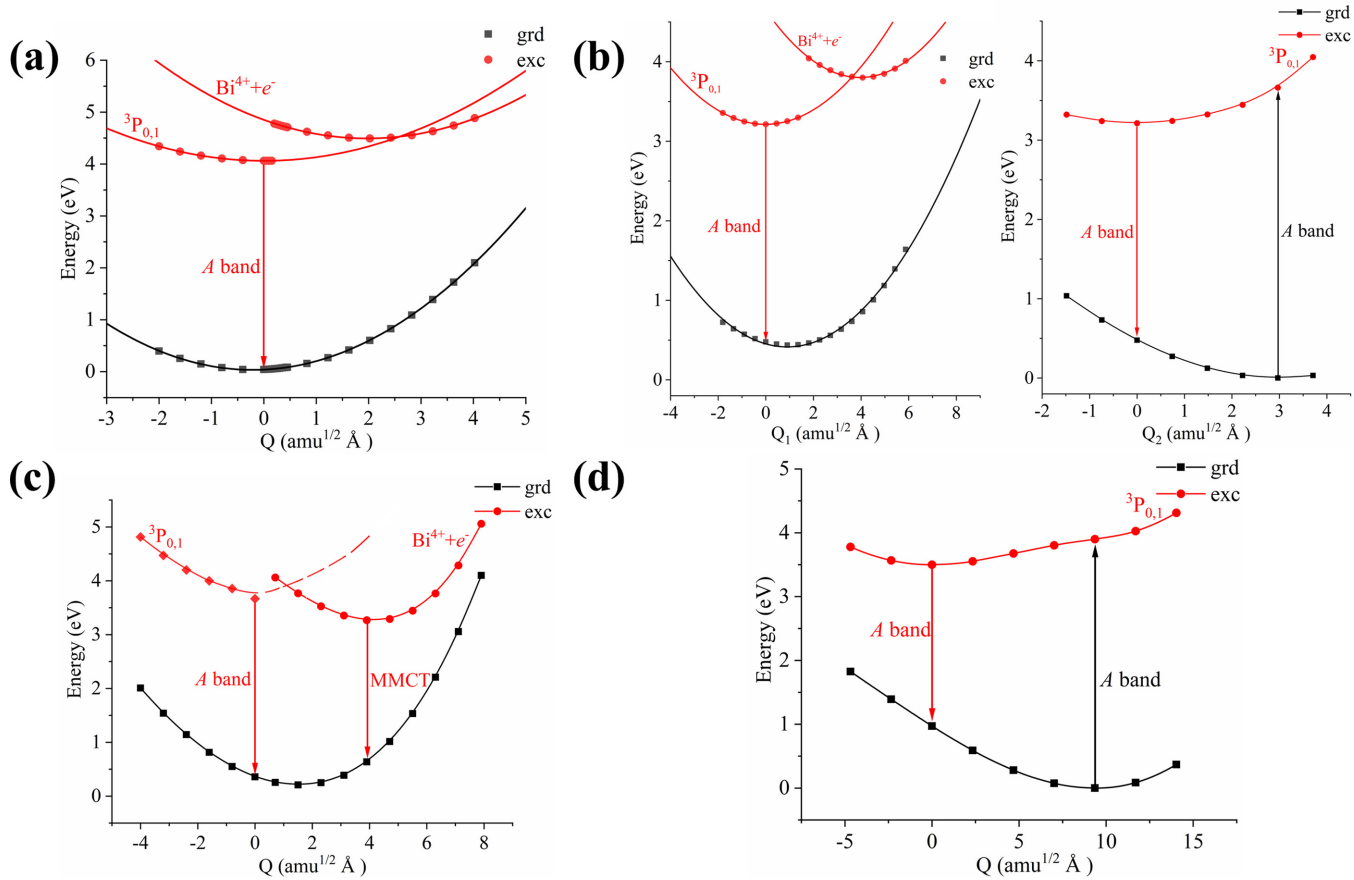

FIG. 10. Configuration coordinate diagrams of the Bi^{3+}-related optical transitions for (a) $CaSb_2O_6$:Bi^{3+}, (b) $Ca_2Sb_2O_7$:Bi^{3+} (site 1), (c) $CaSnO_3$:Bi^{3+}, and (d) $SrGa_2O_4$:Bi^{3+} (site 1), respectively. The mass-weighted configuration coordinate Q in (a), (c) [or Q_1 in (b)] is along the interpolated geometries between two excited-state equilibrium structures, and Q_2 in (b) or Q in (d) is pointing from the structure of the $^3P_{0,1}$ state to the ground state. The vertical axis energy is relative to the energy of the ground state at its equilibrium structure.

TABLE I. Calculated (calc) and measured (expt) excitation (exc) and emission (em) energies (in units of eV) for the Bi^{3+}-related transitions in (Ca/Sr)Sb_2O_6:Bi^{3+}, (Ca/Sr)$_2Sb_2O_7$:Bi^{3+}, (Ca/Sr)SnO_3:Bi^{3+}, and (Ca/Sr)Ga_2O_4:Bi^{3+}. In the case of two sites, the left- and right-hand sides of "/" in "calc" are for sites 1 and 2, respectively.

	Calc				Expt			
	MMCT		*A* band		Emission 1		Emission 2	
Host	exc	em	exc	em	exc	em	exc	em
$SrSb_2O_6$	5.07	4.13	3.89	3.65	4.12 [28]	3.70, 3.89 [c]	3.52, 3.40 [c]	2.55, 2.46, 2.43 [c]
$CaSb_2O_6$	5.07	3.91	4.08	4.02	4.28 [28]	4.18 [28]	3.68/3.69/3.65 [d]	2.80,2.84,2.74 [d]
$Sr_2Sb_2O_7$	/4.09	2.93/2.68	3.24/3.69	2.48[a]/	3.33 [21]	2.49 [21]		
$Ca_2Sb_2O_7$	4.57/4.17	2.96/2.53	3.66/3.73	2.74/	3.57, 3.68 [e]	2.84, 2.83 [e]		
$SrSnO_3$	4.06	2.81	4.33/4.19[b]	3.09[b]	4.13 [37]	3.20 [37]		2.85 [37]
$CaSnO_3$	4.06	2.61	4.05/4.03[b]	3.31[b]	4.07 [34]	3.44 [34]		2.74 [34]
$SrGa_2O_4$	5.41/5.40	3.99/4.35	3.90/3.96	2.53/2.68	3.76 [32]	2.23 [32]		2.49 [32]
$CaGa_2O_4$	5.30/5.36	3.71/3.86	4.03/3.84	2.53/2.89				

[a]CT transition.
[b]Hybrid functional calculation results on the equilibrium configurations obtained with PBE functional.
[c]3.89, 3.52, and 2.55 from [28]; 3.40 and 2.46 from [35]; and 3.70 and 2.43 from [25].
[d]3.68 and 2.80 from [28]; 3.69 and 2.84 from [31]; and 3.65 and 2.74 from [24].
[e]3.57 and 2.84 from [21], 3.68 and 2.83 from [30].

parameters α via the GKT and then evaluate the reliabilities of the mixing parameters α we adopted now for the description of STHs.

Following Ref. [96], the dependence of the GKT-relevant quantities on the Fock-exchange mixing parameters α was investigated by taking the one oxygen STHs in $SrSb_2O_6$, $Ca_2Sb_2O_7$, $SrSnO_3$, and $SrGa_2O_4$ as examples. The STH geometry and the finite-size correction terms [78,98] for total energy $E_{\rm corr}[h^+]$ and single-particle energy $\varepsilon_{\rm corr}[h^+]$, obtained using their respective mixing parameters determined via the reproduction of the optical band gaps, were applied to a range of parameter values. Figure 8 shows the dependence of the $E[N]-E[N-1]$ for the STH and its single-particle energies ($\varepsilon_{\rm ST}[N-1]$ and $\varepsilon_{\rm ST}[N]$) on α. As is shown in Fig. 8, when using the mixing parameters determined via the reproduction of the optical band gaps of the hosts, as the electron is added, $\varepsilon_{\rm ST}[N-1]$ shifts upwards to $\varepsilon_{\rm ST}[N]$. In other words, the functionals we have adopted show convex behavior, promoting hole delocalization to some extent. We find that $\varepsilon_{\rm ST}[N-1]$ and $\varepsilon_{\rm ST}[N]$ almost linearly increase and decrease with increasing α, respectively, while comparatively speaking, $E[N]-E[N-1]$ is weakly dependent of α. The linear fits of the three quantities approximately intersect at $\alpha=0.27$, 0.26, 0.24, and 0.28 for $SrSb_2O_6$, $Ca_2Sb_2O_7$, $SrSnO_3$, and $SrGa_2O_4$, respectively, which are all larger than the mixing parameters we adopted now for each host. Consequently, these mixing parameters determined via the satisfaction of the GKT undoubtedly support the existence of the STHs in these hosts. Moreover, the values of the $E[N]-E[N-1]$ have a relatively small variation from the mixing parameters we adopted now to the GKT-optimized parameters. Actually, $E[N]-E[N-1]$ corresponds to the absolute position of the charge transition level at the given geometric structure. We note that the absolute position here is relative to the electron's electrostatic potential energy in the pristine host. This shows that the calculated STH level or self-trapping energy is reliable for a wide range of α, as long as an appropriate STH geometry and electronic structure are obtained and the absolute VBM position is well reproduced. In addition, the reproduction of the optical band gap is important for a relatively accurate absolute VBM position. Hence, the mixing parameters we have adopted can give a reasonable description for STHs as long as $E[N]-E[N-1]$ is used, at least on the aspects of demonstration of the existence of STHs and the characterization of the stability of STHs. The dependencies of the GKT-relevant quantities on α for the STHs in $CaSb_2O_6$, $Sr_2Sb_2O_7$, $CaSnO_3$, and $CaGa_2O_4$ are also provided in Fig. S6 [65].

Next, we consider the optical transitions involving intrinsic defects and STHs by following the Franck-Condon principle. Defects in insulators can introduce levels in the band gaps or near the band edges, which can play an important role in the intrinsic and long afterglow emissions. Even though the formation energies of intrinsic defects that are calculated based on the PBE functional have been used to identify the primary intrinsic defects and their valences, the well-known underestimation of the band gap at the GGA-PBE level affects the positions of the defect-induced states in the gap, which is insufficient for the reliable evaluation of the role of intrinsic defects in the luminescence processes. Hence, we present the results of the thermodynamic charge transition levels for the primary intrinsic defects in Fig. 7 via the hybrid functional calculations. In practical calculations, the optical charge transition levels following the Franck-Condon principle are raised to determine the optical charge transition energies. The definition of the optical charge transition level is similar to the thermodynamic charge transition level defined by Eq. (1), but now the energy of the final state is calculated using the atomic configuration of the initial state. We note that the conventional corrections for charged supercell are not applicable to the calculation of an optical transition level, as this involves a nontrivial combination of ionic and electronic screening. A correction method for optical transition levels involving defect states calculated with a supercell technique is formulated by Gake *et al.* [79,80]. This scheme allows us to achieve reliable optical transition energies for identifying defect signatures in measured optical spectra.

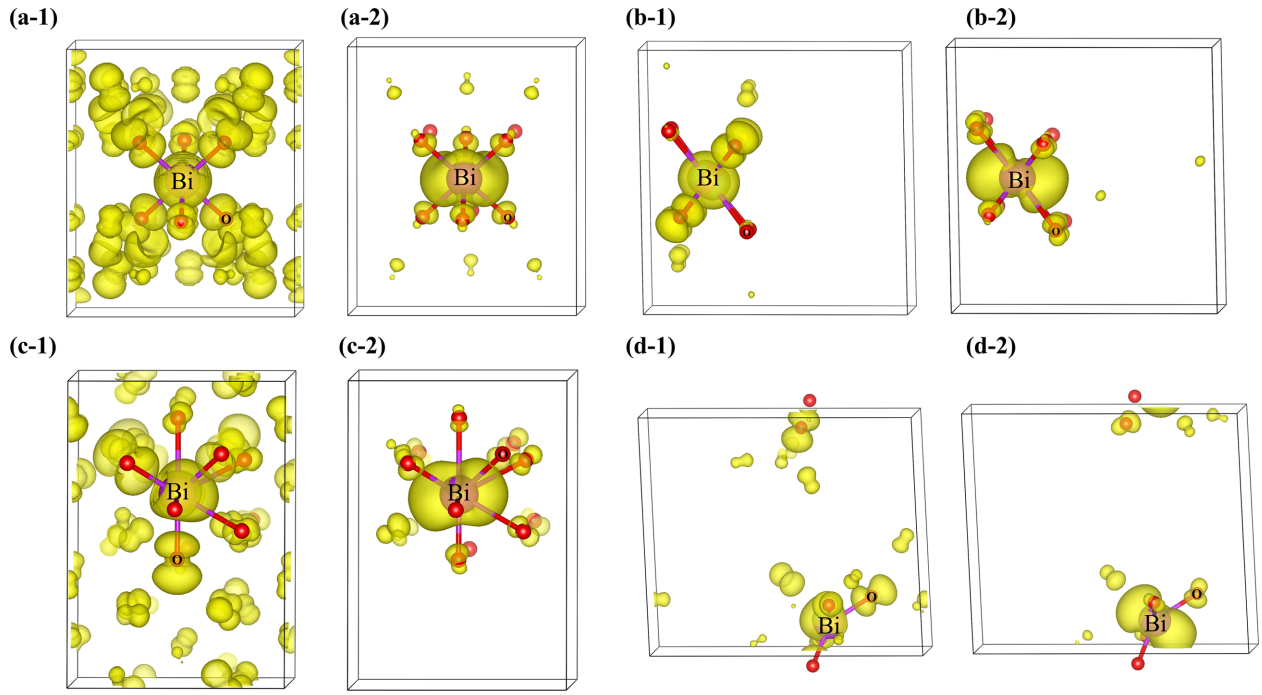

FIG. 11. Partial charge density plots of the hole states [(a-1), (b-1), (c-1), and (d-1)] and electron states [(a-2), (b-2), (c-2), and (d-2) for the excited state of *A*-band transition in (a) $SrSb_2O_6$, (b) $Ca_2Sb_2O_7$ (site 1), (c) $SrSnO_3$, and (d) $SrGa_2O_4$ (site 1), respectively. Notes: For presentation purpose, the isosurfaces correspond to 0.06%, 1.5%, 0.25%, and 1.5% of maximum value for hole states in $SrSb_2O_6$, $Ca_2Sb_2O_7$, $SrSnO_3$, and $SrGa_2O_4$, respectively, while 10% of maximum value for electron states. The smaller thresholds used in (a-1) and (c-1) are merely in order to show the low charge density near the Bi ions.

The calculated peak emission energy for the process $V_{Sr}^{-} + e_{CBM}^{-} \rightarrow V_{Sr}^{2-}$ in $SrSb_2O_6$ is 2.19 eV, which is close to the experimental observed VIS emission peaked at 520 nm under the band-to-band excitation [25,35]. As a result, the V_{Sr}^{2-} is identified to account for the VIS emission observed in $SrSb_2O_6$. Similarly, the optical emission energies involving V_{Ca1}^{2-}, V_{Ca2}^{2-}, Sb_{Ca1}^{+}, Sb_{Ca2}^{+}, Ca_{Sb1}^{3-}, and Ca_{Sb2}^{3-} in $Ca_2Sb_2O_7$ are also calculated, the calculated peak emission energies are 1.47, 1.28, 2.21, 1.61, 1.83, and 0.86 eV for V_{Ca1}^{2-}, V_{Ca2}^{2-}, Sb_{Ca1}^{+}, Sb_{Ca2}^{+}, Ca_{Sb1}^{3-}, and Ca_{Sb2}^{3-}, respectively. Considering the consistency between the calculation results and the experimental data and the formation energies of these intrinsic defects, V_{Ca1}^{2-}, Sb_{Ca1}^{+}, Sb_{Ca2}^{+}, and Ca_{Sb1}^{3-} are all likely to account for the orange emission observed in $Ca_2Sb_2O_7$ under 254-nm excitation [39]. The 440-nm broad blue emission observed in $Ca_2Sb_2O_7$ [40] can be attributed to the recombination of a conduction band minimum (CBM) electron with the STH with predicted emission energy of 2.46 eV. The relatively large self-trapping energy of 0.57 eV makes its presence at room temperature possible. The V_{Sr}^{2-} related optical emission energy in $SrSnO_3$ is also calculated, i.e., 1.77 eV, which is 1.15 eV smaller than the experimental observed blue emission peaked at 2.92 eV [41], making the assignment unlikely. The recombination of an electron from the CBM with the STH is calculated to be 2.82 eV in $SrSnO_3$, remarkably close to the experimental observed blue emission in the host. Furthermore, the relatively low self-trapping energy of 0.37 eV for STH in $SrSnO_3$ in Fig. 7(c) can also explain the temperature dependence behavior of the intrinsic luminescence observed in $SrSnO_3$, i.e., an intense and broad emission band centered at 425 nm at 77 K but no luminescence is observed at room temperature [41]. In $SrGa_2O_4$, the recombination of the electron from the CBM with the STH results in a 2.38-eV emission, close to the optical emission energies involving V_{Sr1}^{2-}, V_{Sr2}^{2-}, and Ga_{Sr1}^{+}, but is 0.67 eV smaller than the peak emission energy, 3.05 eV, of the blue emission observed experimentally in the host [43]. Nevertheless, it is worth noting that the mixing parameter α, which is tuned here in the hybrid functional to reproduce the optical band gap, is not necessarily the most suitable one to describe the properties of STHs. Especially, the calculated self-trapping energy in $SrGa_2O_4$ is 0.89 eV [Fig. 7(d)], which is obviously larger than those in other hosts and implies a significant distortion induced by the STH, and accordingly the increase of the ground-state total energy (Frank-Condon shift) due to the deviation of the STH structure from the ground-state structure is considerable, i.e., 1.96 eV. So we tentatively attribute the blue emission observed in $SrGa_2O_4$ to the STH-related emission, and the large self-trapping energy of the STH in $SrGa_2O_4$ also make it possible to observe the intrinsic emission even at room temperature, rather than the absence of intrinsic blue luminescence at room temperature in $SrSnO_3$. The vertical transition energies of excitation and emission involving primary intrinsic defects in the hosts that under study are listed in Table S5 [65].

In addition, considering the intrinsic emissions peaked at 520 nm for $SrSb_2O_6$ and 654 nm for $Ca_2Sb_2O_7$ are both attributed to the intrinsic defects, as a useful exploration and supplementation, we here attempt to calculate the luminescence line shapes involving these potential intrinsic defects. The calculated spectral densities of the electron-phonon

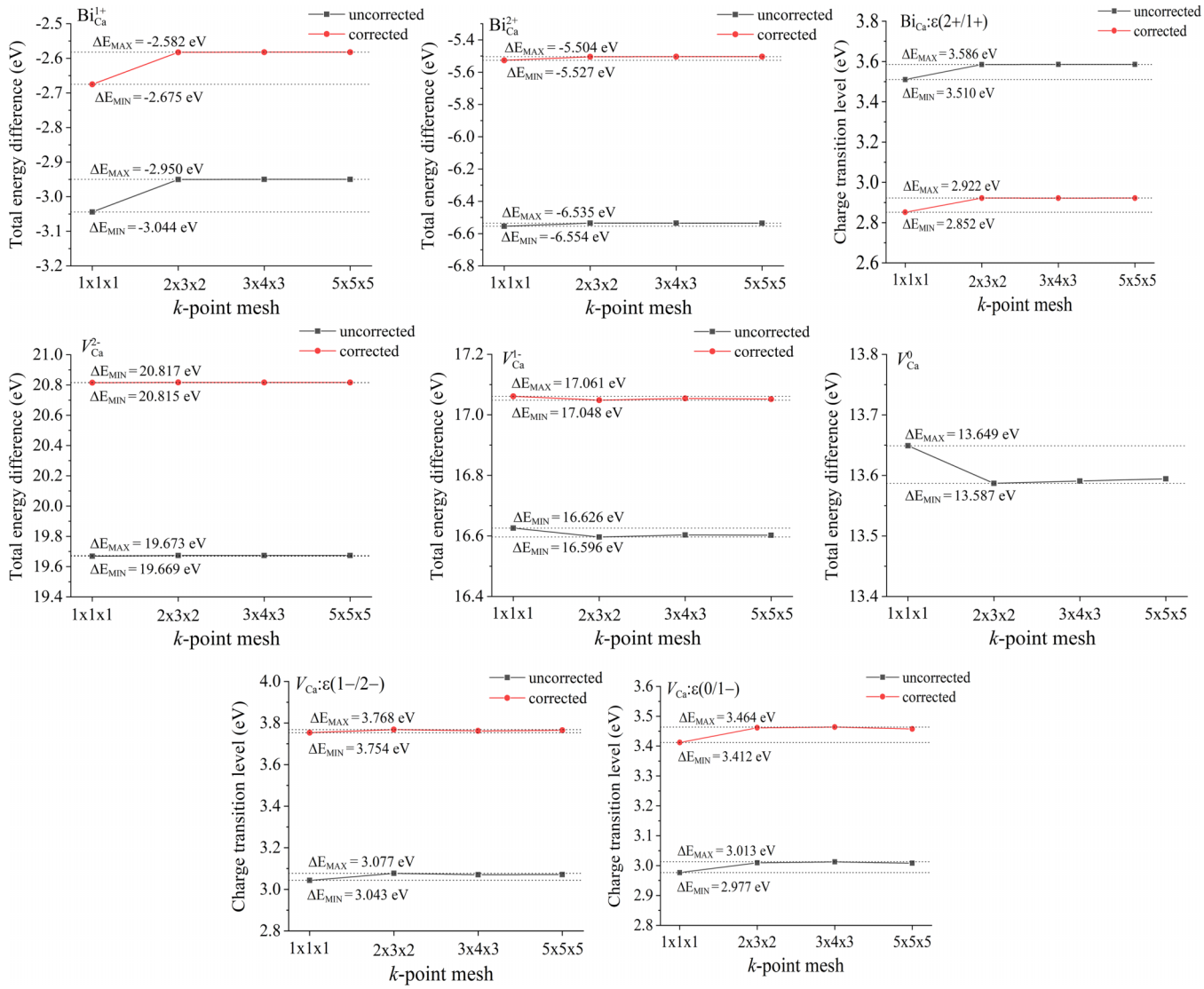

FIG. 12. The k-point sampling convergence test on the Bi_{Ca} dopant and V_{Ca} in $CaSb_2O_6$. Notes: The $2 \times 3 \times 2$, $3 \times 4 \times 3$, and $5 \times 5 \times 5$ k-point meshes correspond to spacing equal to $\sim 0.04 \times 2\pi/\text{Å}$, $\sim 0.03 \times 2\pi/\text{Å}$, and $\sim 0.02 \times 2\pi/\text{Å}$ in all three directions. Notes: The total energy difference is the energy difference between the defected supercell and the pristine supercell.

coupling and the luminescence line shapes for the potential intrinsic defects mentioned before in $SrSb_2O_6$ and $Ca_2Sb_2O_7$ are shown in Figs. (S6) and (S7) [65]. For a more meaningful comparison, we shifted the ZPL of calculated line shapes downward by 0.26 eV for V_{Sr} in $SrSb_2O_6$ and 0.72, 0.13, 0.42, and 0.02 eV for Sb_{Ca1}, Sb_{Ca2}, Ca_{Sb1}, and V_{Ca1} in $Ca_2Sb_2O_7$, respectively, to align the experimental peak emission energies (Fig. S9 [65]). The full width at half-maximums (FWHMs) of these calculated luminescence line shapes are 0.68 eV for V_{Sr} in $SrSb_2O_6$ and 0.50, 0.47, 0.46, and 0.63 eV for Sb_{Ca1}, Sb_{Ca2}, Ca_{Sb1}, and V_{Ca1} in $Ca_2Sb_2O_7$, respectively. And the FWHMs are measured to be 0.85 and 0.43 eV for the experimental observed intrinsic emissions peaked at 520 and 654 nm for $SrSb_2O_6$ and $Ca_2Sb_2O_7$, respectively. The comparison between the calculated and experimental luminescence line shapes shows that the intrinsic defect attributions for the intrinsic emissions observed in $SrSb_2O_6$ and $Ca_2Sb_2O_7$ before are reasonable.

D. Bi^{3+} ion-activated emissions in the hosts

Except for the intrinsic emissions mentioned above, the Bi^{3+}-activated emissions were also much reported in the d^{10} MOs, for example, the UV and green emissions were reported in $SrSb_2O_6$:Bi^{3+}, while the $CaSb_2O_6$:Bi^{3+} gave the UV and blue emissions [24,25,28]; the greenish and blue emissions were reported in $Sr_2Sb_2O_7$:Bi^{3+} and $Ca_2Sb_2O_7$:Bi^{3+}, respectively [21,30]; the UV and VIS emissions were observed in both strontium stannate and calcium stannate [34,37,38]; an asymmetric band peaked at 504 nm is observed under 330-nm excitation in $SrGa_2O_4$:Bi^{3+} [32]. The above-mentioned d^{10} MOs span several crystal systems, which provide different local environments for Bi^{3+} dopants, leading to diverse and rich luminescence phenomena, which bring difficulties to the clear identifications and systematic understanding of the luminescence mechanisms. Furthermore, more than a single doping site in $(Sr/Ca)_2Sb_2O_7$ and $(Sr/Ca)Ga_2O_4$ complicates the analyses and identifications of Bi^{3+}-related transitions. As

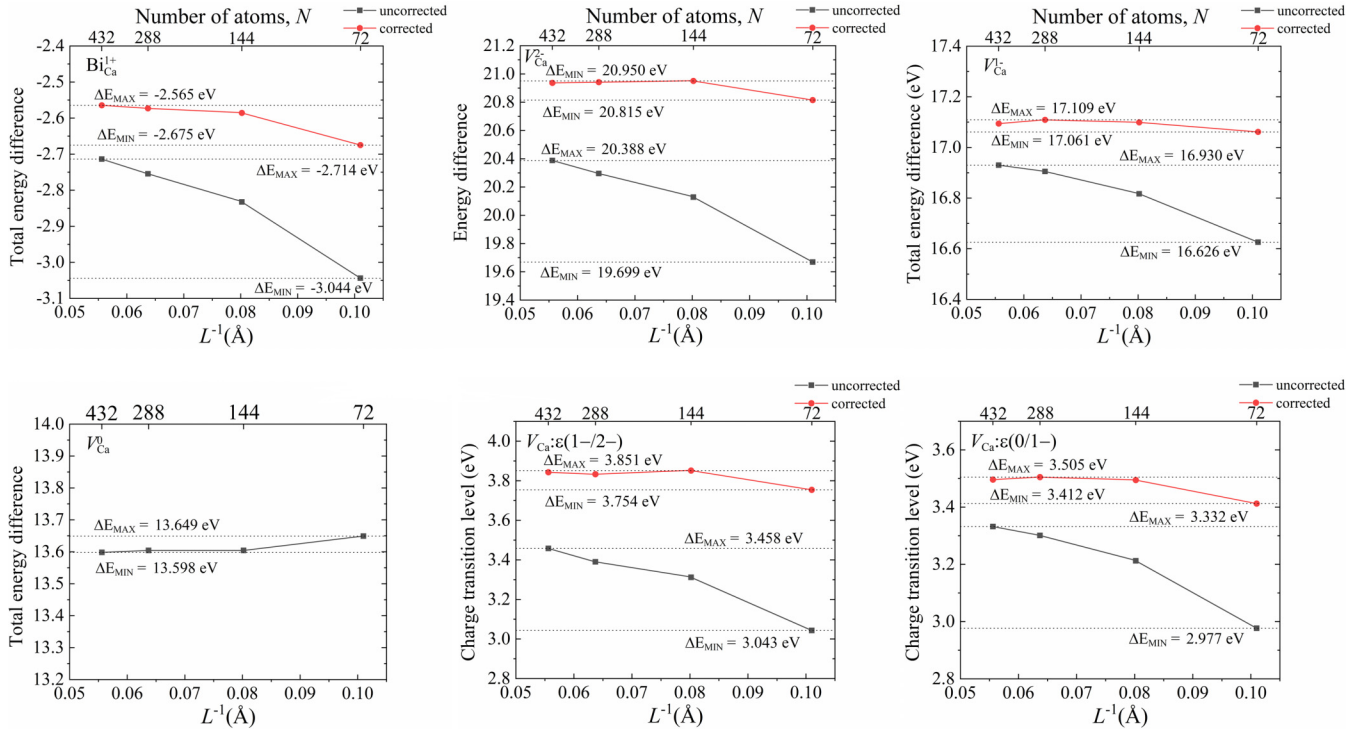

FIG. 13. The supercell size convergence test on the Bi_{Ca} dopant and V_{Ca} in $CaSb_2O_6$. Notes: The distinction can be found between the energy differences and thermodynamic charge transition levels without finite-size correction and those with finite-size correction (eFNV correction), and it is clear that the calculation results with finite-size correction are close to the converged results and are at the order of 0.1-eV level; the total energy difference is the energy difference between the defected supercell and the pristine supercell.

a result, the first-principles calculations show its importance in revealing of the excited-state configurations and the electronic structures of the bismuth dopants which are not accessible in the experimental studies. The independent and valuable insights gained in the first-principles calculations can be used to better understand the luminescence mechanisms of the Bi^{3+} dopants in the d^{10} MOs complemented with the experimental findings.

For the purpose of better presentation and comparison, the thermodynamic charge transition levels of the Bi^{3+} dopants which characterize the trapped levels of the 6*s* and 6*p* characters in the band gaps of the hosts are plotted in Fig. 9 (detailed data obtained by calculations are listed in Table S6 [65]). We have neglected the dopants of Bi_{Ga} and Bi_{Sn}, which have only deep 6*s*-like defect levels (not shown in Fig. 9) and can not account for the bismuth-related transitions. It clearly shows that the $\varepsilon(2+/1+)$ charge transition level of $Bi_{Sr/Ca}$ is in the band gaps for all the d^{10} MOs studied, and so is for the $\varepsilon(1+/0)$ except for the alkaline earth stannates, which possess $\varepsilon(1+/0)$ charge transition levels slightly above CBM. Most of the hole trap levels with the 6*s* character of the hosts studied here are quite shallow in the band gaps, except for the hole traps in $CaSnO_3$ and $Ca_2Sb_2O_7$, which are about 1 eV. This is connected to the compact local structure of Bi_{Ca}: the Ca-O bond lengths in calcium d^{10}-metal oxides are shorter than their strontium counterparts, which push the Bi^{3+}-induced transition levels upward. Consistently, the hole trap level of Bi^{+}_{Sr2} (or Bi^{+}_{Ca2}) locates at higher position than that of Bi^{+}_{Sr1} (or Bi^{+}_{Ca1}) in $Sr_2Sb_2O_7$ (or $Ca_2Sb_2O_7$) due to the shorter average bond lengths of Sr2-O (Ca2-O), while in $SrGa_2O_4$ (or $CaGa_2O_4$), Bi^{+}_{Sr1} (or Bi^{+}_{Ca1}) has the shorter average bond lengths and locates at higher position than that of Bi^{+}_{Sr2} (or Bi^{+}_{Ca2}). This also explains the absence of the $\varepsilon(1+/0)$ electron traps of Bi_{Sr2} in $Sr_2Sb_2O_7$ and Bi_{Ca2} in $Ca_2Sb_2O_7$. However, the presentation of the trap levels in Fig. 9 is not sufficient to give a comprehensive understanding of the Bi^{3+}-related optical transition processes. For example, the $\varepsilon(1+/0)$ charge transition levels of alkaline earth stannates are not in the gaps, however, two emissions of the UV and VIS are still observed in both $SrSnO_3$ and $CaSnO_3$ doped with Bi^{3+}. As a result, the configuration coordinate diagrams (CCDs) are adopted here to characterize the actual dynamics of the Bi^{3+} related transition processes, i.e., *A* band transition ($^1S_0 \leftrightarrow {}^3P_{0,1}$) and MMCT transition ($Bi^{3+} \leftrightarrow Bi^{4+} + e^{-}_{CBM}$). The CCDs can be treated quantitatively based on interpolation between two excited states or between an excited state and the ground state, as shown in Fig. 10.

The generalized configuration coordinate Q is defined as [99]

$$Q^2 = \sum_{\beta,t} m_\beta (R_{\beta t} - R_{i;\beta t})^2, \tag{8}$$

where $\{m_\beta\}$ are atomic masses and Q has a unit of $amu^{1/2}$ Å [amu (atomic mass unit)]. In Fig. 10, $^3P_{0,1}$ is taken as the initial state *i*, and its geometric structure corresponds to $Q = 0$. The geometries of the MMCT excited state ($Bi^{4+} + e^{-}_{CBM}$) and the ground state correspond to different final states with different $Q = \Delta Q$ values given by corresponding changes in

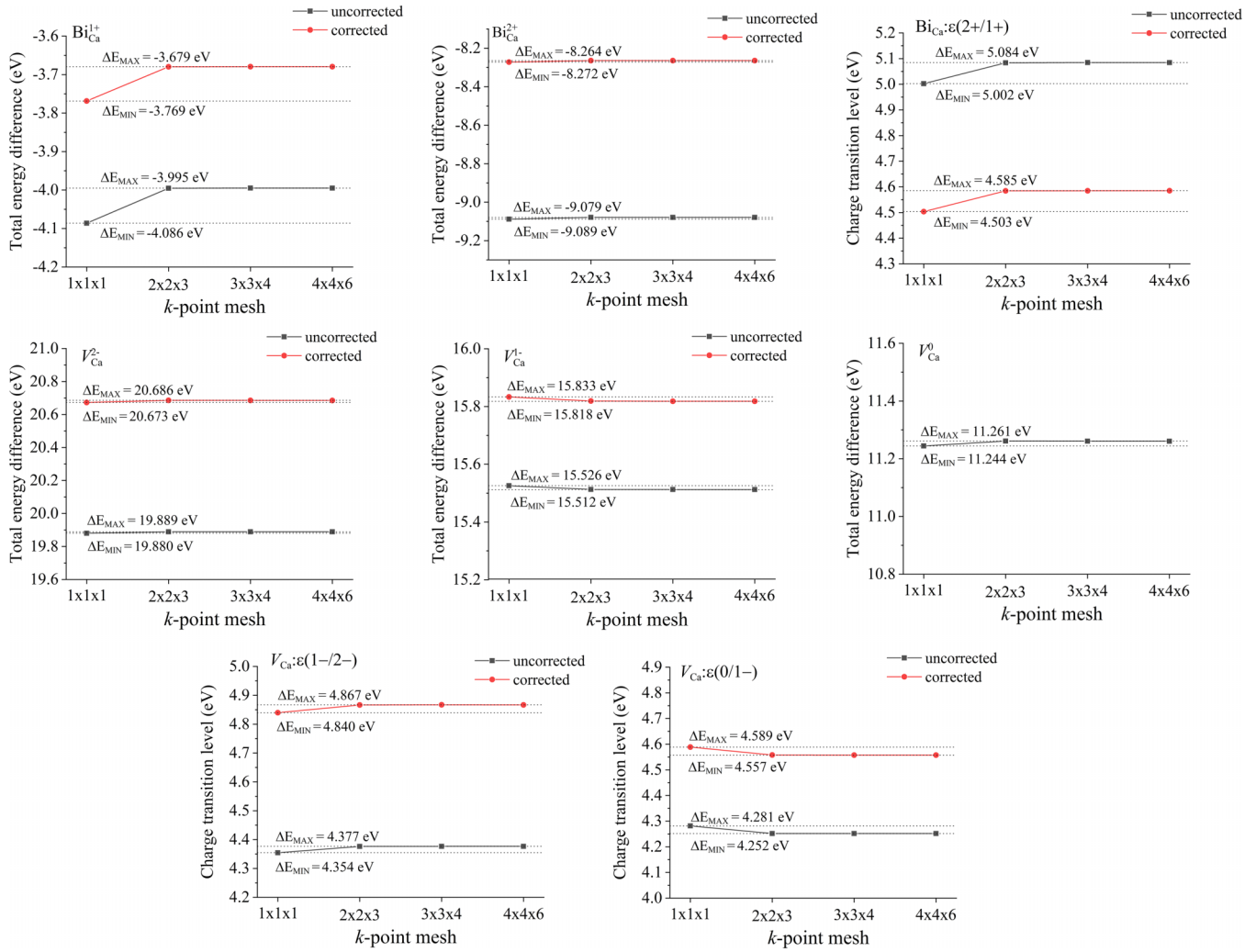

FIG. 14. The k-point sampling convergence test on the Bi_{Ca} dopant and V_{Ca} in $CaSnO_3$. Notes: The $2 \times 2 \times 3$, $3 \times 3 \times 4$, and $4 \times 4 \times 6$ k-point meshes correspond to spacing equal to $\sim 0.04 \times 2\pi/\text{Å}$, $\sim 0.03 \times 2\pi/\text{Å}$, and $\sim 0.02 \times 2\pi/\text{Å}$ in all three directions. Notes: The total energy difference is the energy difference between the defected supercells and the pristine supercell.

atomic coordinates as follows:

$$(\Delta Q)^2 = \sum_{\beta,t} m_\beta \Delta R_{\beta t}^2. \tag{9}$$

The geometric structure $\{R_{\beta t}\}$ of a general state in Eq. (8) is a linear interpolated geometry of the initial state and a given final state (MMCT or the ground state in Fig. 10), leading to a one-dimensional configuration coordinate Q using Eq. (8).

It is worth noting that Bi^{3+} dopants in d^{10} MOs are aliovalent ion doping, so during the calculations of Bi^{3+}-related charge transfer processes, the finite-size corrections including both the image charge correction and the potential alignment correction should be well considered. Similarly, the correction method for optical transition levels developed by Gake *et al.* [80] is applied here. Following the conventional treatment of the dopant-related charge transfer processes [76,100], the Bi^{3+}-related optical charge transition levels are also adopted here to represent the Bi^{3+}-related charge transfer processes. The localized nature of the initial and final states involved in the A band transitions ($^1S_0 \leftrightarrow {}^3P_{0,1}$) make it possible to determine the optical transition energies by applying the ΔSCF method directly following the Frank-Condon principle. The calculation results of the Bi^{3+}-related transition energies in the d^{10} MOs are listed in Table I. The comparison and scrutiny of the calculation results in Fig. 10 and Table I against the available experimental data help us to better identify the Bi^{3+}-related optical transitions. Two emission bands reported with maxima at 510 and 335 nm in $SrSb_2O_6$ were attributed to CT emission and $^3P_{0,1} \rightarrow {}^1S_0$ emission therein [25], respectively. Our calculated emission energy of A band is well consistent with the experimental observed UV emission, but the calculated MMCT ($Bi^{3+} \leftrightarrow Bi^{4+} + e^-_{CBM}$) transition energies locate in the UV range, deviating substantially from the green and blue emissions observed in bismuth-doped $SrSb_2O_6$ and $CaSb_2O_6$, respectively, so are the corresponding excitation energies.

Different from the trigonal crystal system of the alkaline earth metantimonates, the alkaline earth antimonates belong to the orthorhombic crystal system, and give a different luminescence phenomenon compared with that of the alkaline earth metantimonates. Despite the two nonequivalent potential $Sr^{2+}(Ca^{2+})$ sites for Bi^{3+} ions in $Sr_2Sb_2O_7$ ($Ca_2Sb_2O_7$),

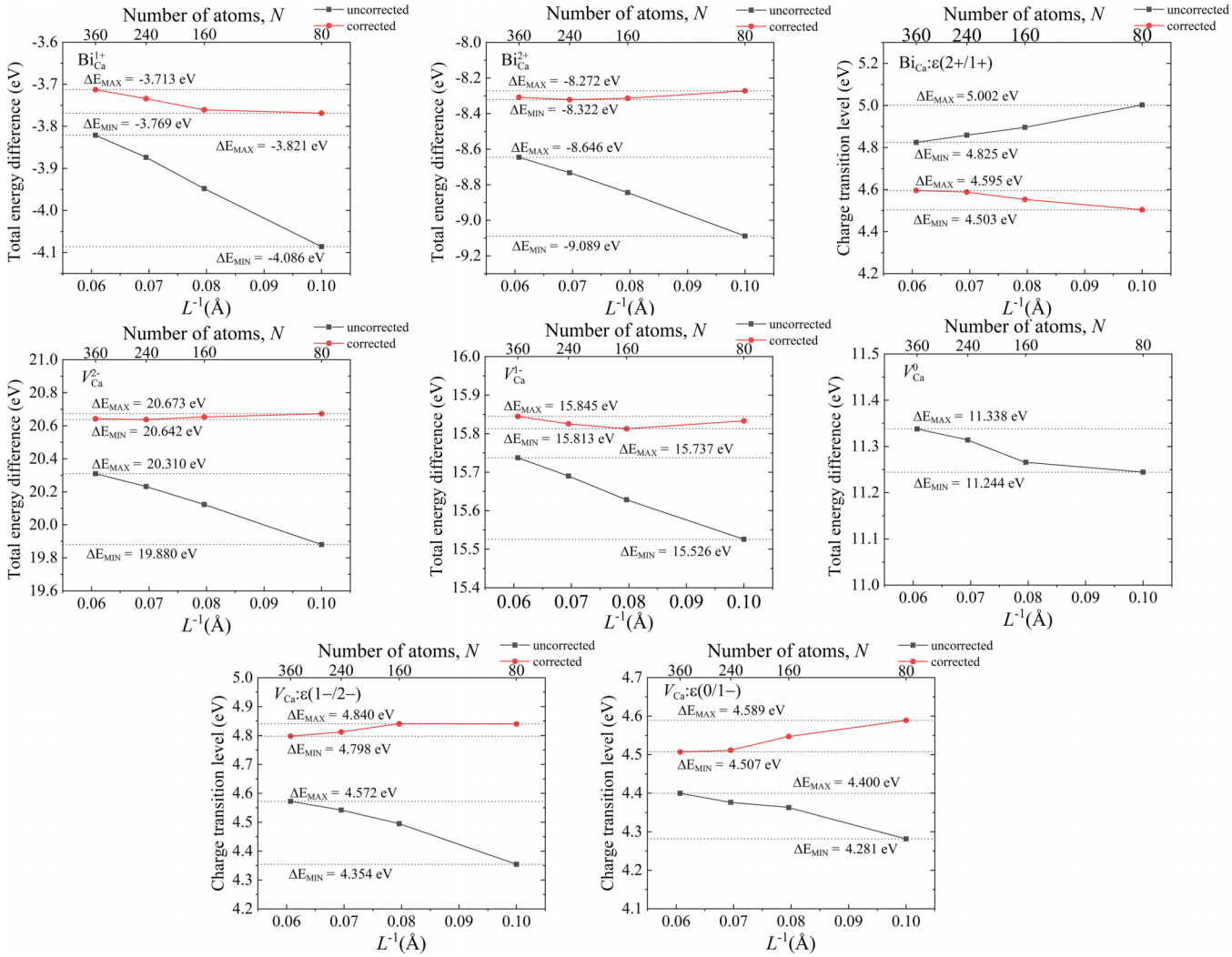

FIG. 15. The supercell size convergence test on the Bi_{Ca} dopant and V_{Ca} in $CaSnO_3$. Notes: The distinction can be found between the energy differences and thermodynamic charge transition levels without finite-size correction and those with finite-size correction (eFNV correction), and it is clear that the calculation results with finite-size correction are close to the converged results and at the order of 0.1-eV level; the total energy difference is the energy difference between the defected supercell and the pristine supercell.

the experimental observed Bi^{3+}-related emissions are symmetric [21], implying the nature of a single emission center. As an obvious comparison, an asymmetric band peaked at 504 nm is observed under 330-nm excitation in Bi^{3+}-doped $SrGa_2O_4$ [32], which also contains two crystallographically nonequivalent Sr^{2+} sites for Bi^{3+} ions. As a result, based on the comparison between measured and calculated peak energies for bismuth-doped $Sr_2Sb_2O_7$ and $Ca_2Sb_2O_7$, and the trend of variation in emission band from $Sr_2Sb_2O_7$ to $Ca_2Sb_2O_7$ in the solid solutions $(Sr_{1-y}Ca_y)_2Sb_2O_7$ [21], the emissions observed in $Sr_2Sb_2O_7$ and $Ca_2Sb_2O_7$ are attributed to Bi_{Sr1}^{+} and Bi_{Ca1}^{+}, respectively. And the Bi^{3+}-related excitations in $(Sr/Ca)_2Sb_2O_7$ are both identified as $^1S_0 \rightarrow {}^3P_{0,1}$ (A-band) transition, while the green and blue emissions observed in $Sr_2Sb_2O_7$ and $Ca_2Sb_2O_7$ are attributed to CT ($Bi^{2+} + h_{VBM}^{+} \rightarrow Bi^{3+}$) and $^3P_{0,1} \rightarrow {}^1S_0$ (A-band) transitions, respectively. The change of emission type from CT ($Bi^{2+} + h_{VBM}^{+} \rightarrow Bi^{3+}$) to $^3P_{0,1} \rightarrow {}^1S_0$ (A band) is also easily understood considering the shallower thermodynamic charge transition level of $\varepsilon(2+/1+)$ for $Sr_2Sb_2O_7$ compared with that for $Ca_2Sb_2O_7$ and the dispersive nature of Bi-6s states. Furthermore, it is interesting to find that the positions and shapes of the green and blue emissions observed in Bi^{3+}-doped $SrSb_2O_6$ and $CaSb_2O_6$ are close and similar to the greenish and blue emissions observed in Bi^{3+}-doped $Sr_2Sb_2O_7$ and $Ca_2Sb_2O_7$, respectively. More surprisingly, the point A in the CPD of $SrSb_2O_6$ shown in Fig. 3(a) corresponds to the coexistence of the $SrSb_2O_6$ and $Sr_2Sb_2O_7$. Similar situations are also expected for $CaSb_2O_6$ and $Ca_2Sb_2O_7$. Thus, we infer that the green and blue emissions observed in Bi^{3+}-doped $SrSb_2O_6$ and $CaSb_2O_6$ originate from the Bi^{3+} dopants in secondary compounds of $(Sr/Ca)_2Sb_2O_7$, which arose during the synthesis processes of $(Sr/Ca)Sb_2O_6$.

When it comes to Bi^{3+}-doped $(Sr/Ca)SnO_3$, the luminescence phenomena and spectral assignments in experiments are clear, the dominant UV emission observed at 10 K in $SrSnO_3$ is attributed to A band transition. As the temperature is increased to $T = 200$ K, the intensity of the UV band decreases in favor of a new VIS emission band centered near 435 nm. And the VIS emission is identified to be the

MMCT transition [37]. Similarly, the dominant broad blue emission peaking near 450 nm in $CaSnO_3$ at room temperature is attributed to the MMCT emission while a weak band near 370 nm which is additionally discerned at low temperature (10 K) is interpreted with *A*-band transition [34]. The distinction on the temperature-dependence behavior between $SrSnO_3$:Bi^{3+} and $CaSnO_3$:Bi^{3+} actually indicates the much smaller energy barrier between *A*-band excited state and MMCT excited state in $CaSnO_3$:Bi^{3+}. Further confirmation and understanding is provided by our calculation results of the Bi^{3+}-related transitions in (Sr/Ca)SnO_3 as is listed in Table I and shown in Fig. 10(c). The calculated *A*-band and MMCT excitation energies are both close to the experimental excitation energies in (Sr/Ca)SnO_3, considering the partially allowed transition nature of the *A*-band excitation, the *A*-band excitation is identified to account for the Bi^{3+}-related excitation in (Sr/Ca)SnO_3. As is shown in Fig. 9, the $\varepsilon(1+/0)$ thermodynamic charge transition levels in (Sr/Ca)SnO_3 both located in positions slightly higher than the conduction band edge states, which lead to difficulty in obtaining the equilibrium structures of their *A*-band excited states. Nevertheless, the hybrid functional calculation results on the PBE-optimized equilibrium configurations of *A*-band excited states presented in Table I still give a well-consistent prediction. Moreover, as is shown in the CCD of $CaSnO_3$ [Fig. 10(c)], the *A*-band excited electronic state for those geometries between $^3P_{0,1}$ equilibrium configuration and $Bi^{4+}+e^-$ equilibrium configuration is hard to be obtained, which also implies the much smaller energy barrier between $^3P_{0,1}$ excited state and MMCT excited state ($Bi^{4+}+e^-$) in $CaSnO_3$:Bi^{3+}.

The asymmetric emission observed in Bi^{3+}-doped $SrGa_2O_4$ implies the two-emission-centers nature, Gaussian decomposition is applied to fit the asymmetric emission profile [32]. The calculation results shown in Table I identify the two emissions of 557 nm (2.23 eV) and 498 nm (2.49 eV) to the *A*-band transition of the Bi^+_{Sr1} and Bi^+_{Sr2} sites, respectively. The calculated *A*-band excitation energies of the Bi^+_{Sr1} and Bi^+_{Sr2} sites are so close to each other that the experimental observed excitation bands are hard to distinguish, so we infer that the Bi^+_{Sr1} and Bi^+_{Sr2} sites both contribute to the excitation bands observed in $SrGa_2O_4$. Besides, it is interesting to find that the Stokes shifts of the *A*-band transitions of Bi_{Sr1} and Bi_{Sr2} sites are $\sim$1.4 and $\sim$1.3 eV, respectively, which are substantially larger than the Stokes shift of a typical *A*-band transition of $\lesssim$1 eV, and are comparable to that of a MMCT transition. The large Stokes shift of the *A*-band transition in $SrGa_2O_4$ is resulted from the obvious bond length changes and the distortion of the coordination environments of the Bi^{3+} ion. By checking the local structures of potential doping sites for bismuth dopant in the hosts (Fig. 1), we observed that only the sites of alkaline ions in (Ca/Sr)Sb_2O_6 are balanced in both bond length and bond angle, giving a small Stokes shift for the *A*-band transition, while those in all the other hosts are imbalanced in bond lengths and angular distribution, especially in (Sr/Ca)Ga_2O_4, allowing a large structure relaxation and giving a large Stokes shift.

Finally, in order to show the excited state of *A*-band transition clearly, the partial charge density plots of the electron and hole states for $SrSb_2O_6$, $Ca_2Sb_2O_7$, $SrSnO_3$, and $SrGa_2O_4$, respectively, are shown in Fig. 11 as examples. It shows that (i) the 6*s* (antibonding) orbitals in $SrSb_2O_6$ [Fig. 11(a-1)] and $SrSnO_3$ [Fig. 11(c-1)] are distributed more balanced in mixing the 2*p* orbitals of the nearest-neighboring oxygen ions, while the other two are much less so; (ii) the 6*p* orbitals in $Ca_2Sb_2O_7$ [Fig. 11(b-2)] and $SrGa_2O_4$ [Fig. 11(d-2)] are close to a polar 6*p* orbital in charge distribution, while the 6*p* orbital in $SrSb_2O_6$ [Fig. 11(a-2)] has a more balanced mixing of different ligand orbitals, and to a lesser extent is that in $SrSnO_3$ [Fig. 11(c-2)]. The isosurface plots of the hole and electron states for *A*-band transition in $CaSb_2O_6$, $CaSnO_3$, and $CaGa_2O_4$ are also provided in Fig. S10 [65], showing similar trends. The imbalanced or oriented distributions of the namely 6*s* and 6*p* orbitals in the excited state make it easy to reduce in energy via structure relaxation, leading to a large Stokes shift of *A*-band emission.

IV. CONCLUSIONS

First-principles calculations are carried out on a series of pristine and Bi-doped ternary alkaline earth d^{10} metal oxides to explore their defect structures and luminescence mechanisms, and the results have been employed to interpret the available experimental photoluminescence processes. The main findings are as follows: (i) The existences of STHs (self-trapped holes) in pristine hosts are revealed, which are also identified to account for the intrinsic blue emissions observed in $Ca_2Sb_2O_7$, (Sr/Ca)SnO_3, and $SrGa_2O_4$. (ii) The primary intrinsic defects under the air atmosphere are revealed, including the $V^{2-}_{Sr/Ca}$, V^{2+}_O and antisites ($Sb^+_{Sr/Ca}$, Sn^{2+}_{Sr}, Ga^+_{Sr}). The vacancy V^{2-}_{Sr} is shown to be responsible for the VIS emission peaked at 520 nm in $SrSb_2O_6$, and the alkaline earth vacancies show great potential as hole trap centers in the long persistent luminescence of d^{10}-MOs. (iii) The optical transitions of Bi^{3+} dopants are identified and clarified. The UV emissions observed in bismuth-doped $SrSb_2O_6$ and $CaSb_2O_6$ are attributed to the *A*-band ($^3P_{0,1} \rightarrow {}^1S_0$) transitions, while the observed VIS emissions are attributed to the emissions of Bi^{3+} dopants in the minute amount of secondary compounds of $Sr_2Sb_2O_7$ and $Ca_2Sb_2O_7$, respectively. The Bi^{3+}-related transitions are also well identified and interpreted in (Sr/Ca)SnO_3 and (Sr/Ca)Ga_2O_4. (iv) The Stokes shift of *A*-band transition is small in $SrSb_2O_6$ and $CaSb_2O_6$, but is much larger in other hosts, particularly in $SrGa_2O_4$, where the value of 1.3 $\sim$ 1.4 eV is even comparable to those of MMCT transitions. The large Stokes shifts are associated with susceptibility to structure distortion, while in (Sr/Ca)SnO_3, they are also partially due to the 6*p* levels being slightly higher than the CBM and prone to mixing with conduction bands. To sum up, the revelation of STHs, the determination of dominant intrinsic defects and the excitations, emissions, and the large variation of the Stokes shifts of Bi^{3+} with different local ligand arrangements should be beneficial for designing and optimizing phosphors based on alkaline earth d^{10} metal oxides.

ACKNOWLEDGMENTS

We thank Q. Quan from University of Science and Technology of China for discussing the calculations of luminescence line shapes. We acknowledge the support of the

National Key Research and Development Program of China (Grant No. 2018YFA0306600), and Anhui Initiative in Quantum Information Technologies (Grant No. AHY050000). The numerical calculations were performed on the supercomputing system at the Supercomputing Center of the University of Science and Technology of China. We have also used VASPKIT [62] and VESTA [101] for the purpose of postprocessing and display of our results.

APPENDIX

To dismiss the possible concern of readers on the convergence of our calculation results, the k-point sampling and size convergence tests on the Bi_{Ca} dopants and V_{Ca} in the $CaSb_2O_6$ (Figs. 12 and 13) and $CaSnO_3$ (Figs. 14 and 15) which are modeled with relatively small supercells in our paper were performed. As is shown in Figs. 12 and 14, the changes of the energy differences between the defected supercells and the pristine supercell and the charge transition levels for Bi_{Ca} dopants and V_{Ca} with respect to the Γ-point calculations were less than 0.1 eV in both $CaSb_2O_6$ and $CaSnO_3$. Similar to the k-point sampling convergence tests, the size convergence tests shown in Figs. 13 and 15 exhibit that the changes of the corrected energy differences between the defected supercells and the pristine supercell and the charge transition levels for Bi_{Ca} dopants and V_{Ca} with respect to the supercells we adopted now were also at the order of 0.1-eV level in both $CaSb_2O_6$ and $CaSnO_3$. Therefore, we considered our calculation results to be converged and were reliable enough to support our conclusions.

[1] D. Liu, X. Yun, P. Dang, H. Lian, M. Shang, G. Li, and J. Lin, Chem. Mater. **32**, 3065 (2020).
[2] X. Li, P. Li, Z. Wang, S. Liu, Q. Bao, X. Meng, K. Qiu, Y. Li, Z. Li, and Z. Yang, Chem. Mater. **29**, 8792 (2017).
[3] L. Liu, S. Peng, Y. Guo, Y. Lin, X. Sun, L. Song, J. Shi, and Y. Zhang, ACS Appl. Mater. Interfaces **14**, 41215 (2022).
[4] Y. Zhang, D. Chen, W. Wang, S. Yan, J. Liu, and Y. Liang, Inorg. Chem. Front. **7**, 3063 (2020).
[5] H. C. Swart and R. E. Kroon, Opt. Mater.: X **2**, 100025 (2019).
[6] B. Lou, J. Wen, J. Cai, Y.-Y. Yeung, M. Yin, and C.-K. Duan, Phys. Rev. B **103**, 075109 (2021).
[7] J. Xue, H. M. Noh, B. C. Choi, S. H. Park, J. H. Kim, J. H. Jeong, and P. Du, Chem. Eng. J. **382**, 122861 (2020).
[8] D. Ruan, Z. Huang, Z. Tang, Y. Zhang, X. Wang, M. Zhou, J. Qi, and T. Lu, J. Phys. Chem. C **124**, 913 (2020).
[9] H. Chen, Y. Gao, P. Jiang, R. Cong, and T. Yang, Dalton Trans. **50**, 4179 (2021).
[10] J. Xue, X. Wang, J. H. Jeong, and X. Yan, Phys. Chem. Chem. Phys. **20**, 11516 (2018).
[11] L. Dong, L. Zhang, Y. Jia, B. Shao, S. Zhao, and H. You, J. Mater. Chem. C **8**, 12231 (2020).
[12] S. Wu, P. Xiong, X. Liu, Y. Fu, Q. Liu, Y. Chao, Q. Dong, Y. Li, W. Chen, Y. Chen, Z. Ma, and M. Peng, J. Mater. Chem. C **9**, 3672 (2021).
[13] B.-M. Liu, Z.-J. Yong, Y. Zhou, D.-D. Zhou, L.-R. Zheng, L.-N. Li, H.-M. Yu, and H.-T. Sun, J. Mater. Chem. C **4**, 9489 (2016).
[14] N. K. Thipparapu, Y. Wang, S. Wang, A. A. Umnikov, P. Barua, and J. K. Sahu, Opt. Mater. Express **9**, 2446 (2019).
[15] P. Gao, Q. Li, S. Li, S. Gai, Y. Li, Y. Ma, Z. Zhang, M. S. Molokeev, Z. Zhou, and M. Xia, J. Phys. Chem. C **126**, 9195 (2022).
[16] S. Wu, P. Xiong, X. Liu, Y. Fu, Q. Liu, M. Peng, Y. Chen, and Z. Ma, J. Mater. Chem. C **8**, 16584 (2020).
[17] F. Locardi, E. Sartori, J. Buha, J. Zito, M. Prato, V. Pinchetti, M. L. Zaffalon, M. Ferretti, S. Brovelli, I. Infante, L. De Trizio, and L. Manna, ACS Energy Lett. **4**, 1976 (2019).
[18] J. Luo, X. Wang, S. Li, J. Liu, Y. Guo, G. Niu, L. Yao, Y. Fu, L. Gao, Q. Dong, C. Zhao, M. Leng, F. Ma, W. Liang, L. Wang, S. Jin, J. Han, L. Zhang, J. Etheridge, J. Wang *et al.*, Nature (London) **563**, 541 (2018).
[19] F. Kang, H. Zhang, L. Wondraczek, X. Yang, Y. Zhang, D. Y. Lei, and M. Peng, Chem. Mater. **28**, 2692 (2016).
[20] T. Lyu and P. Dorenbos, Chem. Eng. J. **372**, 978 (2019).
[21] D. Zhao, Y.-N. Li, R.-J. Zhang, B.-Z. Liu, and Q.-X. Yao, ACS Sustainable Chem. Eng. **9**, 7569 (2021).
[22] S. Firstov, A. Umnikov, A. Kharakhordin, A. Vakhrushev, E. Firstova, S. Alyshev, A. Khegai, K. Riumkin, Y. Ososkov, A. Guryanov, and M. Melkumov, Opt. Lett. **47**, 778 (2022).
[23] B. Jacquier, G. Boulon, G. Sallavuard, and F. Gaume-Mahn, J. Solid State Chem. **4**, 374 (1972).
[24] C. Pedrini, G. Boulon, and F. Gaumemah, Phys. Status Solidi A-Appl. Res. **15**, K15 (1973).
[25] J. de Blank and G. Blasse, ChemInform **27**, 295 (1996).
[26] C. Pedrini, J. Chem. Phys. **63**, 3085 (1975).
[27] P. Boutinaud, J. Lumin. **223**, 117219 (2020).
[28] Y. Xia, F. Huang, W. Wang, A. Wang, and J. Shi, J. Alloys Compd. **476**, 534 (2009).
[29] L. Chen, Y. Long, Y. Qin, and W. Li, Mater. Lett. **102-103**, 59 (2013).
[30] S. Yao, X. Zhou, Y. Huang, Z. Wang, Y. Long, and W. Li, J. Alloys Compd. **653**, 345 (2015).
[31] S. Yao, L. Chen, Y. Huang, and W. Li, Mater. Sci. Semicond. Process **41**, 265 (2016).
[32] T. Wang, X. Xu, D. Zhou, Y. Yang, J. Qiu, and X. Yu, Inorg. Chem. **55**, 894 (2016).
[33] R. Cao, T. Fu, Y. Cao, S. Jiang, Q. Gou, Z. Chen, and P. Liu, J. Mater. Sci.-Mater. Electron. **27**, 3514 (2016).
[34] A. M. Srivastava, Opt. Mater. (Amsterdam) **58**, 89 (2016).
[35] R. Cao, T. Fu, D. Peng, C. Cao, W. Ruan, and X. Yu, Spectroc. Acta Pt. A-Molec. Biomolec. Spectr. **169**, 192 (2016).
[36] S. Wang, W. Chen, D. Zhou, J. Qiu, X. Xu, and X. Yu, J. Am. Ceram. Soc. **100**, 3514 (2017).
[37] A. M. Srivastava, Opt. Mater. (Amsterdam) **72**, 313 (2017).
[38] M. Back, J. Ueda, J. Xu, K. Asami, L. Amidani, E. Trave, and S. Tanabe, J. Phys. Chem. C **123**, 14677 (2019).
[39] G. Blasse and A. Bril, Mater. Res. Bull. **5**, 231 (1970).
[40] A. George, S. Gopi, E. Sreeja, T. Krishnapriya, A. C. Saritha, C. Joseph, N. Unnikrishnan V, and P. R. Biju, J. Mater. Sci.: Mater. Electron. **31**, 423 (2020).
[41] W. Zhang, J. Tang, and J. Ye, Chem. Phys. Lett. **418**, 174 (2006).

[42] M. Tsega and F. B. Dejene, Bull. Mater. Sci. **40**, 1347 (2017).
[43] X. Cai, Z. Mu, S. Zhang, D. Zhu, Q. Wang, Y. Yang, D. Luo, and F. Wu, J. Lumin. **200**, 169 (2018).
[44] D. Ye, Z. Hu, W. Zhang, Y. Cui, L. Luo, and Y. Wang, Opt. Mater. (Amsterdam) **36**, 1879 (2014).
[45] Y. Hua, W. Ran, P. Dang, W. Tian, and J. S. Yu, Int. J. Energy Res. **46**, 7904 (2022).
[46] Y. Wang, P. Feng, S. Ding, S. Tian, and Y. Wang, Inorg. Chem. Front. **8**, 3748 (2021).
[47] C. Zheng and Q. Liu, RSC Adv. **9**, 33596 (2019).
[48] G. Bergerhoff, R. Hundt, R. Sievers, and I. D. Brown, J. Chem. Inf. Comput. Sci. **23**, 66 (1983).
[49] J. P. Perdew, K. Burke, and M. Ernzerhof, Phys. Rev. Lett. **77**, 3865 (1996).
[50] G. Kresse and J. Hafner, Phys. Rev. B **47**, 558 (1993).
[51] G. Kresse and J. Furthmuller, Phys. Rev. B **54**, 11169 (1996).
[52] G. Kresse and J. Furthmuller, Comput. Mater. Sci. **6**, 15 (1996).
[53] G. Kresse and D. Joubert, Phys. Rev. B **59**, 1758 (1999).
[54] H. Mizoguchi and P. Woodward, Chem. Mater. **16**, 5233 (2004).
[55] H. Xue, Z. Li, L. Wu, Z. Ding, X. Wang, and X. Fu, J. Phys. Chem. C **112**, 5850 (2008).
[56] H. Xue, Z. Li, H. Dong, L. Wu, X. Wang, and X. Fu, Cryst. Growth Des. **8**, 4469 (2008).
[57] X. Zhang, H. Guo, Q. Shi, C. e. Cui, Y. Cui, P. Huang, and L. Wang, Ceram. Int. **48**, 36201 (2022).
[58] R. Huang, X. Xu, J. Zhu, W. Liu, R. Yuan, X. Fu, Y. Zhang, and Z. Li, Appl. Catal. B-Environ. **127**, 205 (2012).
[59] Q. Liu, F. Jin, B. Li, and L. Geng, J. Alloys Compd. **717**, 55 (2017).
[60] S. Steiner, S. Khmelevskyi, M. Marsmann, and G. Kresse, Phys. Rev. B **93**, 224425 (2016).
[61] J. P. Perdew, A. Ruzsinszky, G. I. Csonka, O. A. Vydrov, G. E. Scuseria, L. A. Constantin, X. Zhou, and K. Burke, Phys. Rev. Lett. **100**, 136406 (2008).
[62] V. Wang, N. Xu, J.-C. Liu, G. Tang, and W.-T. Geng, Comput. Phys. Commun. **267**, 108033 (2021).
[63] Y. Hinuma, G. Pizzi, Y. Kumagai, F. Oba, and I. Tanaka, Comput. Mater. Sci. **128**, 140 (2017).
[64] A. Togo and I. Tanaka, arXiv:1808.01590.
[65] See Supplemental Material at http://link.aps.org/supplemental/10.1103/PhysRevB.107.085144 for additional results on band structures, projected density of states, formation energies of bismuth dopants, local structure and isosurface plots of the hole wave-function squares of alkaline earth vacancies, the potential energy surfaces between two-oxygen STHs and one-oxygen STHs and their corresponding isosurface plots of the hole wave-function squares, the dependence of the GKT-relevant quantities on the Fock-exchange mixing parameters for the STHs, the electron-phonon spectral functions and line shapes of the photoluminescence with large Stokes shift for potential intrinsic defects which may account for the intrinsic emissions, partial charge density plots of the hole states and electron states for the A-band excited state, the reciprocal lattice vectors of the special k points in the k path for host materials, calculated lattice parameters, static dielectric constants and corresponding point charge corrections, the chemical potential values at vertices in chemical potential diagrams for the hosts under study, excitation and emission energies involving primary intrinsic defects and trap depths of Bi dopants, which contains Refs. [66–72].
[66] B. G. DeBoer, R. Young, and A. Sakthivel, Acta Crystallogr. Sect. C-Cryst. Struct. Commun. **50**, 476 (1994).
[67] A. Bystroem, Arkiv foer Kemi Mineralogi och Geologi **18**, 8 (1945).
[68] L. Chelazzi, T. B. Ballaran, F. Nestola, L. Bindi, and P. Bonazzi, Solid State Sci. **13**, 1092 (2011).
[69] S. Ouni, S. Nouri, J. Rohlicek, and R. Ben Hassen, J. Solid State Chem. **192**, 132 (2012).
[70] N. Takani and H. Yamane, Powder Diffr. **29**, 254 (2014).
[71] F. Jiang, P. Jiang, M. Yue, W. Gao, R. Cong, and T. Yang, J. Solid State Chem. **254**, 195 (2017).
[72] H. J. von Deiseroth and H. K. Müller-Buschbaum, Z. Anorg. Allg. Chem. **402**, 201 (1973).
[73] S. Baroni and R. Resta, Phys. Rev. B **33**, 7017 (1986).
[74] M. Gajdoš, K. Hummer, G. Kresse, J. Furthmüller, and F. Bechstedt, Phys. Rev. B **73**, 045112 (2006).
[75] R. W. Nunes and X. Gonze, Phys. Rev. B **63**, 155107 (2001).
[76] C. Freysoldt, B. Grabowski, T. Hickel, J. Neugebauer, G. Kresse, A. Janotti, and C. G. Van de Walle, Rev. Mod. Phys. **86**, 253 (2014).
[77] C. Freysoldt, J. Neugebauer, and C. G. Van de Walle, Phys. Rev. Lett. **102**, 016402 (2009).
[78] Y. Kumagai and F. Oba, Phys. Rev. B **89**, 195205 (2014).
[79] Y. Kumagai, https://github.com/kumagaigroup/pydefect.
[80] T. Gake, Y. Kumagai, C. Freysoldt, and F. Oba, Phys. Rev. B **101**, 020102(R) (2020).
[81] C. Linderälv, W. Wieczorek, and P. Erhart, Phys. Rev. B **103**, 115421 (2021).
[82] M. Lax, J. Chem. Phys. **20**, 1752 (1952).
[83] R. Kubo and Y. Toyozawa, Prog. Theor. Phys. **13**, 160 (1955).
[84] A. Alkauskas, B. B. Buckley, D. D. Awschalom, and C. G. Van de Walle, New J. Phys. **16**, 073026 (2014).
[85] A. Alkauskas, M. D. McCluskey, and C. G. Van de Walle, J. Appl. Phys. **119**, 181101 (2016).
[86] Y. Jin, M. Govoni, G. Wolfowicz, S. E. Sullivan, F. J. Heremans, D. D. Awschalom, and G. Galli, Phys. Rev. Mater. **5**, 084603 (2021).
[87] A. Togo and I. Tanaka, Scr. Mater. **108**, 1 (2015).
[88] Z. Feng, B. Lou, Q. Chen, M. Yin, C.-G. Ma, and C.-K. Duan, Inorg. Chem. **60**, 16614 (2021).
[89] Y. Inoue, Energy Environ. Sci. **2**, 364 (2009).
[90] Y. Kumagai, N. Tsunoda, A. Takahashi, and F. Oba, Phys. Rev. Mater. **5**, 123803 (2021).
[91] C. Van de Walle and J. Neugebauer, J. Appl. Phys. **95**, 3851 (2004).
[92] L. Wang, T. Maxisch, and G. Ceder, Phys. Rev. B **73**, 195107 (2006).
[93] C. G. Perez-Herenandez, R. Sanchez-Zeferino, U. Salazar-Kuri, and M. E. Alvarez-Ramos, Chem. Phys. **551**, 111324 (2021).
[94] A. Janotti, J. B. Varley, M. Choi, and C. G. Van de Walle, Phys. Rev. B **90**, 085202 (2014).
[95] H. Zhao, M. Shi, J. Zou, B. Yang, Y. Li, Z. Wang, and C. Chang, Ceram. Int. **43**, 2750 (2017).

[96] T. Gake, Y. Kumagai, and F. Oba, Phys. Rev. Mater. **3**, 044603 (2019).

[97] J. P. Perdew, R. G. Parr, M. Levy, and J. L. Balduz, Phys. Rev. Lett. **49**, 1691 (1982).

[98] S. Falletta, J. Wiktor, and A. Pasquarello, Phys. Rev. B **102**, 041115(R) (2020).

[99] A. Alkauskas, Q. Yan, and C. G. Van de Walle, Phys. Rev. B **90**, 075202 (2014).

[100] J. L. Lyons, A. Janotti, and C. G. Van de Walle, Appl. Phys. Lett. **95**, 252105 (2009).

[101] K. Momma and F. Izumi, J. Appl. Crystallogr. **44**, 1272 (2011).